Geological and geochemical constrains on the genesis of the sedimentary-hosted Bou Arfa Mn(-Fe) deposit (Eastern High Atlas, Morocco)

Lafforgue, Ludovic; Dekoninck, Augustin; Barbarand, Jocelyn; Brigaux, Benjamin; Bouabdellah, Mohammed; Verhaert, Michele; Mouttaqi, Abdellah; Yans, Johan

Published in:
Ore Geology Reviews

DOI:
10.1016/j.oregeorev.2021.104094

Publication date:
2021

Document Version
Version created as part of publication process; publisher's layout; not normally made publicly available

Journal Pre-proofs

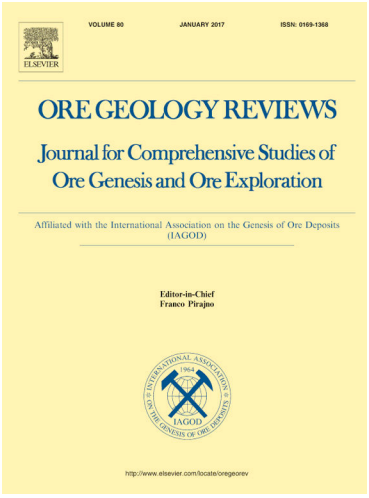

Geological and geochemical constrains on the genesis of the sedimentary-hosted Bou Arfa Mn(-Fe) deposit (Eastern High Atlas, Morocco)

Ludovic Lafforgue, Augustin Dekoninck, Jocelyn Barbarand, Benjamin Brigaud, Mohammed Bouabdellah, Michèle Verhaert, Abdellah Mouttaqi, Johan Yans

PII: S0169-1368(21)00119-0
DOI: https://doi.org/10.1016/j.oregeorev.2021.104094
Reference: OREGEO 104094

To appear in: *Ore Geology Reviews*

Received Date: 17 December 2020
Revised Date: 19 February 2021
Accepted Date: 1 March 2021

Please cite this article as: L. Lafforgue, A. Dekoninck, J. Barbarand, B. Brigaud, M. Bouabdellah, M. Verhaert, A. Mouttaqi, J. Yans, Geological and geochemical constrains on the genesis of the sedimentary-hosted Bou Arfa Mn(-Fe) deposit (Eastern High Atlas, Morocco), *Ore Geology Reviews* (2021), doi: https://doi.org/10.1016/j.oregeorev.2021.104094

Geological and geochemical constrains on the genesis of the sedimentary-hosted Bou Arfa Mn(-Fe) deposit (Eastern High Atlas, Morocco)

Ludovic Lafforgue[1], Augustin Dekoninck[2,@], Jocelyn Barbarand[1], Benjamin Brigaud[1], Mohammed Bouabdellah[3], Michèle Verhaert[2], Abdellah Mouttaqi[4], Johan Yans[2]

[1]Université Paris-Saclay, CNRS, GEOPS, 91405, Orsay, France.

[2]Institute of Life-Earth-Environment (ILEE), University of Namur, 61 rue de Bruxelles B-5000, Namur, Belgium.

[3]Département de Géologie, Faculté des Sciences, Université Mohammed Premier, Avenue Mohammed VI, BP 717, 60000 Oujda, Morocco.

[4]Office national des Mines et des Hydrocarbures, BP 99 Rabat, Morocco.

Ludovic Lafforgue: ludovic.lafforgue.c@gmail.com

Augustin Dekoninck (corresponding author): augustin.dekoninck@unamur.be

Jocelyn Barbarand: jocelyn.barbarand@u-psud.fr

Benjamin Brigaud: benjamin.brigaud@u-psud.fr

Mohammed Bouabdellah: mbouabdellah2002@yahoo.fr

Michèle Verhaert: michele.verhaert@hotmail.com

Abdellah Mouttaqi: MOUTTAQI@onhym.com

Johan Yans: johan.yans@unamur.be

Abstract

Carbonate-hosted Mn deposits are widespread in North Africa with most of the Mn ores being hosted by Mesozoic dolomitic formations of the Moroccan Atlasic system. The Bou Arfa Mn(-Fe) deposit described herein is located in the eastern High Atlas, close to the North Atlasic Front, and has accounted for the production of ~2 Mt of ore grading from 33 to 82% Mn. The mineralization occurs within Sinemurian flat-lying dolostones as stratabound and karst-filling (veins, lenses, pockets). This mineralization is characterized by the extensive presence of pyrolusite, and minor concentrations of manganite, hausmannite, goethite and hematite. Previous studies suggested that the Bou Arfa Mn-bearing mineralization has a strictly synsedimentary origin, but the intense dolomitization and the occurrence of Mn oxides instead of Mn carbonates question this model. New petrographical, mineralogical and geochemical data show that three dolomitization phases accompanied the ore formation. The early synsedimentary dolomitization was not responsible for strong Mn enrichments, whereas a second dolomitization took place with the formation of hausmannite and manganite during early diagenesis. The precipitation mechanism involves circulation of dissolved Mn^{2+} in pore waters, and then precipitation under diagenetic suboxic and alkaline conditions. The scarcity of Mn carbonates is likely due to competitiveness of dissolved carbonates species that have favored dolomite precipitation in the early stage. Presence of saddle dolomite in a subsequent alteration stage, crystallography of the Fe oxides, and evolution of $\delta^{13}C$ and $\delta^{18}O$ reflect burial diagenesis and fluid mixing in the carbonate host rock. These conditions have enabled the transformation of the primary ore into pyrolusite, when diagenetically-derived hydrothermal fluids have generated vein-filling ore. The position of the Bou Arfa site above a paleohigh formed during Atlas rifting, the presence of a faulted zone and the dolomitization of the Sinemurian series have delimited the extension of this diagenetic Mn deposit, which is in some points similar to MVT deposits of North Africa. Weathering is poorly recorded in the Bou Arfa Mn ores due to the stability of the ore-forming minerals under subaerial conditions in relation to the most recent periods of exposure of the High Atlas building.

Keywords: manganese, Bou Arfa, diagenesis, Morocco, sedimentary-hosted

1. INTRODUCTION

Sedimentary-hosted Mn deposits are considered as the most significant amongst different ore deposit types, because they ensure high longevity, large tonnage, and relatively high average grades (Kuleshov, 2016; Laznicka, 1992; Maynard, 2014; Roy, 2006). The accumulation of Mn in sediments is generally triggered by the formation of (i) ferromanganese nodules above the ocean floor (Glasby, 2006; Maynard, 2014; Wang and Müller, 2009), or (ii) Mn-bearing carbonates under diagenetic conditions, either from precipitation in pore waters, or by replacement of Mn-rich oxides, oxyhydroxides and hydroxides (hereafter referred to as Mn oxides; Johnson et al. 2016). Mn sources in sediments can be either distant hydrothermal vents or hydrogenous (terrigeneous) influxes (Fleet, 1983; Glasby, 2006). Formation models (Calvert and Pedersen, 1996; Cannon and Force, 1983; Force and Cannon, 1988; Force and Maynard, 1991; Maynard, 2014, 2010) involve the precipitation of primary Mn oxides at the interface between reducing and oxidizing environments. Most of these oxides are not deposited in deep sediments because they are dissolved again once they deepen in the water column, unless the seafloor is shallow enough to intercept the redox boundary. Iron is not involved in this process as Fe remains fixed in sulfide minerals at the deeper water-sediments interface (Maynard, 2014, 2010). Sea level changes may have a strong influence on the concentration and the geometry of Mn orebodies (Roy, 2006). Most of the sedimentary-diagenetic Mn deposits are hosted in C-rich shales and pelites (Kuleshov, 2016, 2011; Roy, 2006).

The Bou Arfa Mn deposit of the eastern High Atlas of Morocco (Fig. 1A) is located at the junction between the High Atlas and the High Plateau domain close to the North Atlasic Front (Fig. 1B). The Bou Arfa mineralization was discovered in 1912 and is the third Mn district of Morocco alongside the Imini-Tasdremt (Dekoninck et al., 2016a, 2020; Gutzmer et al., 2006) and the Ouarzazate mining districts (Choubert and Faure-Muret 1973; Pouit 1980; Fig. 1A). Previous works have shown that mineralization mainly occurs as stratabound and karst-fill within Sinemurian dolostones (Fig. 2). Their mineralogy consists exclusively of Mn oxides such as pyrolusite (β-MnO_2; Pouit and Jouravsky 1965). Vein-related Mn mineralization is also described and displays massive Fe oxides (goethite) alongside the Mn oxides. The dolomitized host rocks are enriched up to 1–3% Mn and Pouit and Jouravsky (1965) suggested that the carbonate host rocks constitute the source of manganese.

These features interestingly suggest the intervention of processes different from those involved in giant sedimentary-diagenetic deposits (Johnson et al., 2016; Kuleshov, 2016; Maynard, 2014, 2010; Roy, 2006). These high-grade Mn ores occurring in a restricted area would imply epigenetic processes related to dolomitization. Pouit and Jouravsky (1965)

suggested a two-step model to explain the evolution of the Mn mineralization after replacement of a synsedimentary carbonate precursor and their oxidation. However, this model remains questionable (du Dresnay, 1965; Michard and Raddi, 2011; Pouit and Jouravsky, 1965). Accordingly, the genesis of Bou Arfa Mn mineralization needs an in-depth revision in order to address issues related to the syn-sedimentary, diagenetic and/or hydrothermal origin of the orebodies; the link with dolomitization of the host Sinemurian marine carbonates; the massive presence of Mn oxides instead of Mn-rich carbonates (kutnohorite, rhodochrosite or Mn-rich calcite) and the role played by supergene processes. The main objectives of this paper consist of (1) refining the mineralogy and petrography of the Mn mineralization and host carbonates, and (2) defining the relation between the ore formation and host carbonates. The final aim is to propose a robust metallogenic model for the Bou Arfa deposit and special care is devoted to the link between mineralization and dolomitization.

2. REGIONAL AND LOCAL GEOLOGICAL SETTING

The Atlasic fold and thrust belt is a complex structure resulting from the inversion of Triassic and Jurassic basins in the frame of the Africa-Europe convergence (Choubert and Faure-Muret 1962; Mattauer et al. 1977; Fig. 1A). Two main faults border the chain: the northern main thrust named the “North Atlasic Front” (NAF) and the “South Atlasic Fault” (SAF). The chronology of the Atlasic building follows two main phases: Eocene and Plio-Quaternary (Frizon de Lamotte et al., 2009, 2000). A third Miocene phase is identified due to lithosphere thinning that supports the current topography of the Anti-Atlas, the High and the Middle Atlas (Gouiza et al., 2017, 2017; Leprêtre et al., 2015; Missenard et al., 2008, 2006; Seber et al., 1996).

The Bou Arfa area is located in the eastern part of the High Atlas, close to the NAF. The host rocks correspond to Paleozoic schists undetermined in age unconformably overlain by a thick pre-rift Triassic succession, and Jurassic and Cretaceous syn-rift sediments. The Jbel Bou Arfa (1830m; Fig 1B) forms an E-W anticline crossed by a major E-W fault (Aïn Beida fault; du Dresnay 1965). This structure separates the Atlasic system in the south from a non-deformed domain forming the so-called “High Plateaus” in the north (Fig. 1B). Triassic to Jurassic Atlasic basins are rift basins controlled by normal faults and represent transfer zone between two opening domains, namely the Central Atlantic and Tethyan oceans (Fig. 1A; Frizon de Lamotte et al. 2000). The E-W Aïn Beida fault is a main regional structure that split the Bou Arfa area in two blocks: the northern block hosts the Ain-Beida and Hamaraouet Mn mineralization, whereas the southern block hosts small Mn spots (Fig. 1B).

In the Bou Arfa Mn deposit, Sinemurian series are dolostones interbedded with clays and thin gypsum-rich sandstones (Choubert and Faure-Muret 1962; du Dresnay 1965; Salahane 1978; Fig. 2). Two main dolostone units are observed (Fig. 2). The bottom dolostone called Lower “Chocolate” Unit (LCU) because of its dark brownish color is a few meters thick and displays clayey levels in the upper part (du Dresnay 1965; Fig. 2). The second unit, called the Upper “Chocolate” Unit (UCU), is a massive dolostone composed of several strata hosting evaporitic levels, with a cumulated thickness increasing from west to east (10 to 30 meters thick; du Dresnay 1965). Both are separated by an arkose level. In Bou Arfa, the Pliensbachian unit unconformably overlays the Sinemurian rocks with 180 m to 200 m of arkoses, in which granitic boulders are observed (Fig. 2).

The Lower Cretaceous rocks are only observed north of the NAF and form a thin reddish detrital layer. Cretaceous limestones few meters thick form the Kif El Hamar relief and corresponds to an E-W syncline following the Aïn Beida Fault (Fig. 1B). No Mn deposit is observed in these two reliefs but Pb-Zn-Cu-V mineralization have been described (Fig. 1B; Verhaert et al. 2017, 2018). Cenozoic conglomeratic lenses outcrop close to the Aïn Beida Fault (Fig. 1B). These lenses are witnesses of the late Cenozoic activity of the Aïn Beida Fault (Lafforgue, 2016).

3. MATERIAL AND ANALYTICAL METHODS

3.1. Sampling strategy and methodology

The Hamaraouet cliff offers a large domain of outcrops, where most of the samples were collected (Fig. 1B). Mineralized orebodies and host rocks were sampled in the Hamaraouet area (H1 to H4, 26 samples), in the gallery 63 (HB1, 3 samples) and in the Aïn Beida site (6 samples; Fig. 1B; Table 1). Reference stratigraphic log and host rock samples are described in barren carbonates at Hamaraouet, where neither Fe, nor Mn oxides were observed (Fig. 2).

3.2. Analytical methods

The petrography of the samples was carried out using optical microscopy, cathodoluminescence (CL) microscopy (OPEA), scanning electron microscopy (SEM) and Raman-microspectrometry on 70 thin sections prepared in the GEOPS laboratory (Orsay, France). The description of hand specimens (Table 1) was used to select representative samples for geochemical analyses and specific mineral phases from the different stages defined in the paragenesis. ICP-AES and ICP-MS on bulk samples and EPMA on individual minerals were used for the geochemistry. Carbon and oxygen isotope geochemistry

performed on carbonate phases (calcite and dolomite) was undertaken to characterize the source and evolution of paleofluids.

3.2.1 Petrography

Thin sections were observed with an optical microscope Leica at a magnification between x25 and x100 in plane polarized light (PPL) and in cross-polarized light (CPL). Cathodoluminescence observations were made with a *Cathodyne* platine under an acceleration voltage of 10 to 15 kV and a current intensity from 250 to 400 mA. Exposure time was approximately 800 msec for dolomite and seconds for calcite. Texture and optical characteristics have been used to define the different dolomite phases in the mineralized zone. A SEM Phillips XL30 coupled with an Energy Dispersive Spectrometer (EDS) detector Synergie4 PGT was used for petrographical observations and semi-quantitative analyses under an acceleration potential from 15 to 25 kV and probe current of 1.5 nA.

3.2.2 X-ray diffraction (XRD)

XRD analyses were used to distinguish or correlate mineral phases, especially pyrolusite and Fe oxyhydroxide mineral species. XRD data were acquired in the GEOPS laboratory using a PANalytical X'Pert PRO diffractometer with X'Celerator detector and a copper anticathode providing Cu $K\alpha_1$ emission ray. A Ni filter of 0.02 mm was used upon the receptor. Analyses were realized on disoriented powder. All results were treated with X'pert HighScore 3.0e in order to avoid induced $K\alpha_2$ rays.

3.2.3 Raman microspectrometry

Raman microspectrometry analysis was carried out at the University of Lille 1 (France) in the CGCE laboratory. A Horiba Jobin-Yvon spectrometer equipped with an Ar^+ laser was used with a wavelength of 532 nm. A long acquisition time was needed for Mn oxyhydroxides (~30 sec; Julien et al. 2004; Gao et al. 2009). The Ar laser spot size was between 1–2 µm with variable power (max 92 mW). A filter (D1) was used in order to limit the power at 9.2 mW and in order to avoid phase changes due to the laser power. Raman spectra were further treated with the CrystalSleuth software using the Rruff database. Peak parameters were obtained with pseudoVoigt modelisation with fityk 0.8.0 software.

3.2.4 Geochemistry

3.2.4.1 Bulk-rock analysis

Twenty-five samples were analyzed as powders after crushing with an agate mortar at the SARM laboratory (Nantes, France). An ICP-AES Jobin-Yvon JY 70 Type II was used for

major elements (Si, Al, Fe total, Mn total, Mg, Ca, Na, K, P, Ti and LOI). Trace elements and rare earth elements were analyzed with an ICP-MS Perkin Elmer ELAN 5000 (Tables 2 and 3). Samples were heated at 1000 °C (fire loss) and then treated by Li tetraborate fusion to determine the Lost On Ignition (LOI). Samples were analyzed after an acid dissolution (ICP-AES) or a dilution (ICP-MS). Standards were routinely analyzed under the same procedure. The data were compared to the Upper Continental Crust composition (Mc Donough and Sun, 1995) to show up enrichment or depletion. This standard was chosen as it represents the best approximation for the types of rock involved in the mineralizing process at Bou Arfa.

3.2.4.2 Electron Probe Microanalysis

An Electron Probe Microanalysis (EPMA) CAMECA SX-Five was used for quantitative analyses at the University Pierre-et-Marie-Curie of Paris (UPMC) in the Camparis Service. EPMA is equipped with a LaB_6 source and five Wavelengths Dispersive Spectrometers (WDS) coupled with a Bruker EDS. Acceleration potential was 15 kV and variable probe current were used for the identification of minor (low current) and major elements (high current). Standards and probe current are indicated in the data repository (DR1). Analyses were performed on the different dolomite generations (210 spots), on the Mn (217 spots; pyrolusite, hausmannite, cryptomelane, hollandite and chalcophanite) and the Fe (105 spots; hematite and goethite) oxides (Tables 4, 5 and 6).

3.2.5 Stable Isotope geochemistry

The $\delta^{13}C$ and $\delta^{18}O$ compositions of carbonates were obtained at the Radiometric Dating and Stable Isotope Research laboratory at the University of Kiel (Germany). Samples were formerly collected using a micro-drill tool after an in-depth cathodoluminescence characterization. Carbon and oxygen isotopic compositions were determined using 100% H_3PO_4 dissolution at 75 °C with a prototype Kiel 1 unit attached to a Thermo Finnigan MAT 251 mass spectrometer. The results are given in the standard δ-notation, which is expressed relative to V-PDB (Vienna Pee Dee Belemnite) for carbon isotopes and V-SMOW (Vienna Standard Mean Ocean Water) for oxygen isotopes in permil (‰; Table 7). The reproducibility of the analyses of in-house standards gave an external precision (1SD) of ± 0.02‰ for $\delta^{18}O$ and 0.01‰ for $\delta^{13}C$.

4. RESULTS

4.1 Dolomitization

Dolomitization is the main form of wall-rock alteration and three stages are distinguished: (i) extensive syn-sedimentary to early diagenetic replacement dolomite, (ii) epigenetic ore-stage

and (iii) hydrothermal dolomite superimposed on the diagenetic dolostone (Fig. 4). Regional dolomitization predates mineralization and significantly enhances porosity and permeability of the host rock. Ore-related dolomites occur as pore-filling or veins crosscutting the host dolostone.

4.1.1 Barren Upper Chocolate Unit (UCU)

Three facies are recognized in the Upper Chocolate Unit (UCU; from bottom to top): (i) sandy dolostone, (ii) massive fine-grained dolostone and (iii) bedded dolostone with bird eyes (Fig. 2). (i) The UCU starts with a thin level (<50 cm thick) displaying a high proportion of detrital elements including quartz, K-feldspar, and muscovite with subordinate apatite and Ti oxides. These elements are cemented by an anhedral coarse-grained dolomite (Fig. 3A). CL exhibits a red color in the dolomite crystals. (ii) The main facies of the UCU, where most of the ore is located, is formed by a massive dolostone. The lower facies consists of a coarse dolostone where sedimentary textures (pellets, ooliths and pisoliths) are partly preserved (Fig. 3B), and partially replaced by well-developed cloudy microsaccharoïdal to millimetric planar dolomite crystals (Fig. 3C). Pisoliths have a single to multiple-nuclei structure with lightly colored columnar microbial laminations. No Mn- or Fe-rich ooliths (or nodules) nor laminations are observed. (iii) In the upper facies of the UCU, bird eyes are the main feature (Fig. 3D). This level is composed of a micritic brownish dolomite, similar to the dolomite of the bottom detrital level and of the well-preserved part of the massive dolostone level. Bird eyes are filled by a clear sub-planar dolomite with a dark reddish luminescence, while dolomitic cloudy rhombs coating bird eyes have a red luminescence. A small detrital fraction (quartz, feldspar, Fe-Ti oxides, apatite, zircon) is also observed. On top of this level, a dedolomitized limestone (Figs. 3E and F) is observed beneath the unconformity with Pliensbachian arkoses (Fig. 2).

At distance from the mineralized zone — ~4 km south of the Aïn Beida fault in the Jbel Bou Moktha — (Fig. 1B), the Sinemurian series display a well-exposed platform margin system with a north-south lateral facies evolution from (1) lagoonal peloidal-oncoidal dolostones to (2) bioclastic/oolitic grainstones (shoal) and finally to (3) marl/limestone alternation (upper slope). This outcrop in the Jbel Bou Moktha allows to precisely locate the bioclastic/oolitic shoal, protecting the lagoon to the open marine environment. At this location, the lateral equivalent of the UCU only displays an early generation of micritic dolomite followed by several calcite cements (Figs. 3G and H).

4.1.2 Carbonates phases associated to the ores

The three ore-related dolomite phases are not observed outside the mineralized area. Table 8 shows the key identification criteria for the dolomite phases.

4.1.2.1 Early diagenetic dolomite phase (Dol-1)

The earliest dolomitic phase (labeled Dol-1a) replaces calcite precursor, here peloids or ooids. Dol-1a is micro-saccharoidal with red color in CL (Figs. 3A and B). Dol-1b precipitates around Dol-1a with a similar luminescence, unzoned in CL (Fig. 3B). Dol-1a and Dol-1b are the most common carbonate phases.

4.1.2.2 Ore-related epigenetic to hydrothermal dolomite phases (Dol-2 and Dol-3)

Coarse grain dolomite phases (Dol-2 and Dol-3) are intimately related to the highly recrystallized part of the massive dolostone and to the mineralization (Figs. 3C). None of these dolomites occur in the unmineralized zone. Dol-2a is a cloudy dolomite related to the dissolution of sedimentary elements in the massive dolostone and forms mostly planar to sub-planar rhombs with size of ~10–20 µm, cloudy in PPL and bright orange, unzoned in CL. Dol-2a is intrinsically associated with another phase (Dol-2b), which is likely related to the alteration of Dol-2a as shown by impregnation of Dol-2b into Dol-2a (Figs. 3C). Dol-2b is a void and vein filling dolomite, much clearer than Dol-2a in PPL, and characterized by well-developed (hundred microns) sub-planar to non-planar rhombs, bright greenish-yellowish zoned in CL. Dol-2b is a blocky cement but is also connected to veinlets (Fig. 3C).

The last dolomite phase (Dol-3) is observed as cement and vein- or breccia-filling. Dol-3a replaces Dol-2b and forms either a clear dolomite in PPL and dark in CL, or a dark cloudy dolomite (Fig. 3C), bright red-orange unzoned in CL (Fig. 3F). Dol-3b is a clear sub-planar to non-planar (saddle) coarse (hundred microns) rhomb dolomite. A zoned to unzoned dark reddish luminescence characterizes Dol-3b.

4.1.2.3 Late meteoric calcite phases

Late calcite phases also occur across the whole sedimentary series filling the remaining porosity and cutting-across the host dolostone as mm-sized veins. Two generations of calcite are distinguished. The first one (Cal 1) displays yellowish color in CL with zoned scalenohedron crystals in fractures and as replacement of a former dolomite crystal (dedolomite). The second (Cal 2) postdates Dol-3 and is extinct in CL forming sparitic to anhedral crystals in fractures or in breccia (Fig. 3E and 3F).

4.2 Ore mineralogy and petrography

Crosscutting relationships and mineral assemblages indicate the presence of two distinct stages of Mn mineralization (Fig. 4). Veins systematically crosscut both the replacement and karst mineralization. Hausmannite and manganite crystals are crossed or replaced by pyrolusite and later by goethite. It suggests the existence of a prior mineralization related to the formation of Mn(II) and Mn(III) oxides and the existence of two Fe oxyhydroxide stages (Gth1 and Gth2).

4.2.1. Macroscopic features of the Mn-Fe mineralization

From 1922 to 1966, the Bou Arfa manganese deposit was one of the main Mn producers in Morocco with a final production of about ~2 Mt Mn (Mouttaqi et al., 2011). The Mn ore produced metallurgic Mn (33% Mn, 17% Fe) and chemical Mn (82% Mn, <3% Fe; Pouit 1964, 1980; Pouit and Jouravsky 1965; Michard and Raddi 2011; Mouttaqi et al. 2011). The mine remains closed since the seventies. The main mining site is located at Aïn Beida with significant underground works (Figs. 1 and 3). The ore is also well exposed along the Hamaraouet cliff (Figs. 1B and 5A), which constitutes an erosion limit between the basement and the cover; minor mining activities are still in place but galleries in the Upper Chocolate Unit (UCU) are preserved (Figs. 5A and B). From Aïn Beida to Hamaraouet, the Mn mineralization occurs as: (1) a continuous 1-6 meters thick stratabound orebody (~2 km) by replacement of the UCU (Fig. 5C), and (2) veins, stockworks, breccia karst-like (pockets, lenses, cluster) mineralization filling open spaces (Figs. 5D-H; Pouit and Jouravsky 1965; Pouit 1980). This second mineralization is the most important in terms of tonnage and grade. It intensifies toward the core of the Bou Arfa anticline (Fig. 1B) and follows a NE-SW direction parallel to Atlasic directions. It can be subdivided into three sub-groups:

(i) The main sub-type is a prismatic karst-like mineralization forming vertical pipes formerly attributed to the “run-type” ore (Pouit and Jouravsky, 1965). This mineralization is ~100 m long and corresponds to karst collapse structure composed by dolostone blocks embedded in the Mn-Fe mineralization (pyrolusite, manganite, psilomelane, goethite and hematite) and secondary Mn carbonates (Mn-calcite and rhodochrosite). Their main axis follows an ENE direction. According to Pouit and Jouravsky (1965), veins of various sizes (Figs. 5F and 5G) and Mn stockworks (Fig. 5H) are also connected to this mineralization.

(ii) Tabular karst-like mineralization (Fig. 5C) are ten meters long and wide with a thickness of several meters. It follows a sedimentary discontinuous/erosive surface in the upper part of the massive dolostone level of the UCU (Fig. 2) and corresponds to a network of metric channels, parallel to the Sinemurian dolostone strata.

(iii) Finally, local veins are described through the Upper Pliensbachian sandstone. Despite the local specificity of this poorly extended mineralization, Pouit and Jouravsky (1965) indicate that it is likely related to a main fault. Impregnation of stratabound pyrolusite is related to this vein (Figs. 5F and 5G).

The Bou Arfa mineralization is a mixed Mn-Fe type (25% Mn, 10-12% Fe in the bulk ore) dominantly composed of pyrolusite with manganite in the deeper zone, and locally coronadite group minerals (coronadite, hollandite and cryptomelane). Goethite and hematite are systematically present, sometimes forming massive veins (Fig. 5F). Gangue minerals are Mn carbonates, quartz, calcite and barite (Pouit, 1980).

4.2.2 Replacement mineralization

The replacement mineralization is mainly composed of pyrolusite (Fig. 5C), crosscutting and replacing Dol-1b or Dol-2 (Fig. 6A). Pyrolusite occurs as elongated cleaved prismatic crystals with bipyramidal sections (Fig. 6B). Several micrometric disoriented needles of pyrolusite filling voids are present at the base of prismatic pyrolusite crystals (Fig. 6C), which means at least two generations of pyrolusite. Pyrolusite grows onto sub-planar to non-planar altered crystals of Dol-2b. Dol-3b cements pyrolusite (Fig. 6B).

Raman peaks of pyrolusite (Julien et al., 2002, 2004) are identified with a broad shape around 538 ± 5 cm^{-1} and 750 ± 5 cm^{-1} (Fig. 6D). An additional peak close to 630 ± 5 cm^{-1} is also measured. The peak broadening and the presence of an additional peak at 630 ± 5 cm^{-1} are characteristic of slight deviations of the lattice and especially to de Wolff defects corresponding to additional corner-sharing $[MnO_6]^{8-}$ octahedra (such as in 1×2 tunnel oxide structure; de Wolff 1959; Julien et al. 2002). Other phases are also present in the stratabound orebodies such as colloform Fe oxides (goethite) and some phyllosilicates (smectite or biotite in EDS analyses). Colloform goethite crystals are surrounded by micro-pyrolusite (Fig. 6E).

4.2.3 Karst and vein-related mineralization

The Hamarouet karst mineralization is mainly composed of Mn oxides and to a lesser extent of Fe oxyhydroxides. Hausmannite forms euhedral crystals crosscut by Dol-3 (Figs. 7A and B). Hausmannite is ribbed by cleaved pyrolusite crystals that fill fissures with cryptomelane (7A and B). Hausmannite is replaced by chalcophanite or cryptomelane (Figs. 7A and B). The iron mineralization is composed of centimeter rubbed dark goethite (with hematite) crosscut by calcite. This mineralization has a colloform habit and evolves to micro specular at the borders of the Mn ore (Fig. 7E). Fe oxyhydroxides also form a continuous uniform reddish level surrounding lenticular mineralization and are mostly related to the

prismatic karst (Fig. 5G). These reddish levels are composed of micro disoriented needles of pyrolusite replacing large Dol-2b rhombs.

Colloform early manganite (γ-MnOOH) occurs as planar crystals of ten to a hundred microns (Figs. 7C and D). These crystals form lenticular masses with rare hausmannite and barite crystals (Fig. 7D). Manganite is only observed in Aïn Beida.

Carbonate phases are also associated to the Mn-bearing ore minerals and are similar to those observed in the host-rock. Dol-2b, Dol-3 and late calcite phases are observable (Figs. 3F, 7A and B). The late stage calcite is also associated with the precipitation of P-rich minerals (apatite) and some phyllosilicates (smectite or biotite; Fig. 3E). Dol-2b crisscrosses manganite-hausmannite phases at Aïn Beida, when Dol-3 fills voids (Fig. 7A) and surrounds hausmannite. In Aïn Beida area a late Ca-rich rhodochrosite, partially replacing manganite and Dol-2b crystals is observable (Fig. 7C and D).

4.2.4 Crystallinity of the Fe oxides

According to the Scherrer formulation (Langford and Wilson, 1978; Scherrer, 1918), the average size of the crystallite populations of hematite and goethite ranges between 0.02 and 0.12 µm in the whole dataset (Fig. 8). These values were measured at the maximum width of each crystal or in the middle of the crystal and are in good agreement with different studies (Cornell and Schwertmann, 2003; Gualtieri and Venturelli, 1999; Rendon et al., 1983; Schwertmann et al., 1985). The crystallite size of hematite in the stockwork mineralization of Bou Arfa is close to a proto-hematite. This type of hematite is a non-stoichiometric phase, which is characteristic of the transformation by dehydration of goethite into hematite beyond 140 °C in laboratory experiments (Gualtieri and Venturelli, 1999; Pomiès et al., 1998; Walter et al., 2001; Wolska and Schwertmann, 1989; Wolska and Szajda, 1988). This proto-hematite is not an authigenic phase and possesses two distinct groups of crystallites (Lima-de-Faria, 1963). Schwertmann et al. (1985) have shown that the dimension of the a-cell parameter is a witness of the formation temperature of goethite. A long distance (4.626±0.005A) refers to a low temperature of formation (4–40°C), whereas a shorter dimension (4.610±0.001A) corresponds to higher temperatures (50–90°C). The cell dimensions of four Bou Arfa goethites (Table 9) recovered from the reticular distance of planes (200), (040) and (111) are close to a synthetic goethite crystallized at 50 °C. It is also worth noting that a decrease in the peak intensity of 2.45A is characteristic of goethite formed at >40 °C (Schwertmann et al., 1985), which is actually the case in Bou Arfa goethite (see DR2).

4.3. Geochemistry

383 4.3.1 Mineral chemistry

384 *4.3.1.1 Carbonates*

385 EPMA results on dolomite and calcite are reported in Table 4 and plotted in Fig. 9. All
386 the dolomitic phases show excess Ca (26.3 wt.% to 37.8 wt.%; Figs. 9A and B; Table 4). No
387 significant variation is observed to distinguish most of the different generations of dolomites
388 (Figs. 9A and B). Only vein-filling Dol-3 significantly differs from the others, as it contains the
389 highest MnO content (between 1.21 and 9.03 wt.%; Table 4). MnO enrichment implies that
390 late dolomite is close to kutnohorite. It is worth emphasizing that although FeO content (0.13
391 to 1.11 wt.%; Table 4) is lower than MnO, the absolute FeO/MnO ratio is lower than for most
392 of the sedimentary dolomites (Fig. 9C; Searl and Fallick 1990; Montanez and Read 1992;
393 Gasparrinia et al. 2003; Fu et al. 2006). The total amount of trace elements slightly
394 decreases from Dol-1 to Dol-3. The Sr concentration is lower than common marine
395 carbonates (Brand and Veizer, 1980; Zenger et al., 1980). The two late calcite phases are
396 also distinguished, one is Fe-rich, whereas the other is Mn-rich.

397 *4.3.1.2 Manganese oxides*

398 Hausmannite displays minor amounts of SiO_2 (0.05 to 0.30 ± 0.01 wt.%), ZnO (0.05 to
399 2.08 ± 0.02 wt.%) and Fe_2O_3 (0.55 to 1.55 ± 0.24wt.%). Other elements such as Na_2O, MgO,
400 Al_2O_3 or SrO are present at very low concentrations. As hausmannite is commonly replaced
401 by chalcophanite (Fig. 6F), some of the EPMA compositions may be affected.

402 The composition of pyrolusite is heterogeneous. All pyrolusite contain substantial
403 amounts of Al_2O_3 (5.75 ± 0.03 wt.%), SiO_2 (2.11 ± 0.03 wt.%) and CaO (2.25 ± 0.05 wt.%).
404 Only the late-stage pyrolusite grains contain significant amounts of MgO (0.06-1.63 wt.%)
405 and K_2O (0-2.27 wt.%). Pyrolusite in stratabound ores (gallery 63) shows a low CaO content
406 (0.20 ± 0.06%) and the highest Al_2O_3 (0.89 ± 1.12 wt.% to 1.30 ± 0.53 wt.%). All the vein-
407 related pyrolusite have a homogeneous composition.

408 EPMA analyzes also reveal that coronadite group minerals – here represented by
409 hollandite and cryptomelane following the nomenclature of Biagioni et al. (2013) –,
410 concentrate Ba, Sr, K, Ca and Mg (Table 5). K, Ba and Mg are the dominant cations and only
411 hollandite is observed as a pure end-member. Chalcophanite sometimes displays very low
412 Zn concentration, instead of Mg, which could be dominant (up to 4.89 wt.%).

413 *4.3.1.3 Goethite and hematite*

414 All analyzed hematite and goethite samples are from Hamaraouet (Fig. 1B). The total
415 Fe_2O_3 content is abnormally low for goethite and hematite (Table 6) in comparison with their

ideal formula. The total Mn_2O_3 and SiO_2 contents delimit two geochemical trends: (i) The massive colloform goethite and the Fe oxides associated with dedolomitization are enriched in Mn_2O_3 (mean values from 1.46 ± 0.24 to 2.30 ± 0.10 wt.%; Table 6) with minor SiO_2 (mean values from 0.11 ± 0.06 to 0.49 ± 0.47 wt.%) and; (ii) The goethite in veins are enriched in SiO_2 (mean values from 1.71 ± 0.14 to 3.50 ± 0.4 wt.%) with minor Mn_2O_3 content (mean values from 0.09 ± 0.01 to 0.16 ± 0.02 wt.%; Table 6). Goethite and hematite also exhibit minor concentrations of Al_2O_3, MgO, CaO, P_2O_5 and K_2O (ranging from 0.02 to 0.75 wt. %).

4.3.2 Bulk-rock and Mn-ore geochemistry

The Sinemurian dolostones display similar geochemical patterns irrespective of the dolomitizing event that affected these rocks (Fig. 10A). The presence of detrital phases such as quartz, feldspars, zircon, monazite and Ti-oxides explains some high immobile and lithophile contents. One of the striking features in all samples is the higher MnO content (0.74 to 4.71 wt.%) comparative to FeO (0.26% to 1.44 wt.%; Fig. 10A; Table 2). The enrichment in As is also significant.

The karst Mn ores of Aïn Beida, the stratabound Mn and Fe orebodies and the fracture-filling Fe-Mn mineralization show a similar geochemical signature despite their different mineralogy (Figs. 10A and B). Geochemical patterns are close to those of the host rock but with relatively higher enrichments. Lithophile (V), chalcophile (Pb, Zn, Cu) and siderophile (Co, Ni, Mn) elements are more enriched than in the host rock (Fig. 10A). Ba, As, Zn and Fe contents differ between samples: higher Ba and As contents are recorded at Aïn Beida. The Mn/Fe ratio of samples from Aïn Beida (Mn/Fe_{AB1} = 66.9; Mn/Fe_{AB2} = 1.3, Table 3) is also one of the lowest. The late supergene weathered ores are enriched in Sr (1316 to 2350 ppm), Zn (1446 to 2136 ppm) and K_2O (0.66 to 0.96 wt.%), likely due to the presence of hollandite, cryptomelane and chalcophanite. Concentration in lithophile, immobile elements and in REE are low compared to the host rock (Fig. 10A).

The enrichments of the Fe-rich ores are roughly the same as for the Mn ore with some increase in V, As and Pb in the vein-related hematite of Hamaraouet (Fig. 10B). This mineralization is also enriched in Be (6 to 114 ppm) and Ge (2 to 124 ppm). The Fe ore has also a high Mn content up to 0.14-1.07 wt.% Fe_2O_{3t} (Table 3).

Overall, As and Mn are enriched in both the host dolostone and in the mineralization (Tables 2 and 3). Paleozoic schists are depleted in Mn (0.02 wt.% MnO). Chalcophile elements (As, Pb, Zn, Cu) are abundant in the Mn ores and in most of the Fe ores (Fig. 10A and B; Table 3).

4.3.3 Carbon and oxygen isotopic compositions of carbonates

The analyzed carbonates show a wide range of carbon and oxygen isotopic compositions with $\delta^{13}C_{VPDB}$ and $\delta^{18}O_{VSMOW}$ ratios ranging from -8.6 to 2.2‰ and 17.3 to 29.8‰, respectively (Fig. 11; Table 7). $\delta^{18}O_{VSMOW}$ and $\delta^{13}C_{PDB}$ ratios for the primary Dol-1 phase are rather homogenous clustering around 29.2‰ and 29.8‰ for $\delta^{18}O_{VSMOW}$ and 0.1‰ to 2.2‰ for $\delta^{13}C_{VPDB}$. Later dolomite phases (Dol-2 and Dol-3) display $\delta^{18}O$ values from 17.3‰ to 28.6‰ VSMOW and $\delta^{13}C$ values ranging from -7.8‰ to 2.1‰ VPDB. Based on $\delta^{13}C$ values, there is a slight distinction between the Dol-2 cement in the host rock (average value: -0.04 ± 0.40‰ VPDB) and the heavier $\delta^{13}C$ values of the vein filling Dol-2 (mainly represented by Dol-2b; average value: 1.01 ± 0.95‰ VPDB; Fig. 11). Vein-filling Dol-3 shows the lightest $\delta^{13}C$ values (Fig. 11). Some values are heavier, but this may likely be due to impurities in Dol-2 during the analysis. For Dol-2 and Dol-3, both $\delta^{13}C$ and $\delta^{18}O$ values evolve simultaneously towards lighter isotopic values. Late calcite cements display values ranging from 19.5 to 23.1‰ for $\delta^{18}O$ and from -8.5 to -6.1‰ for $\delta^{13}C$ (Fig. 11).

5. DISCUSSION

5.1. Paragenetic sequence

The formation of the Mn(-Fe) ores of Bou Arfa can be summarized in three main stages: (i) Mn-Fe protore, (ii) main Mn-Fe ore and (iii) post ore (Fig. 4). The second stage is economically the most important accounting for most of the extracted Mn ore in the Bou Arfa district, which is mainly expressed by the occurrence of massive pyrolusite. The multistage deposition of Mn-bearing minerals was accompanied by several dolomitization synchronous with the first two stages of Mn deposition (Fig. 4).

5.1.1 Mn-Fe protore

Manganite and hausmannite (Figs. 6F, 7A, B, C) accompany Dol-2, along with colloform to specular Mn-rich Fe oxyhydroxides (goethite and hematite) and barite (Fig. 4). This early Mn(-Fe) mineralization is mainly observed in the Aïn Beida site (Fig. 1B), but the occurrence of hausmannite in the Hamaraouet area also indicates that early stage of mineralization has a larger extension.

5.1.2 Main Mn ore

Fracture-filling and karst mineralization are later than Dol-2. Pyrolusite is the only Mn oxide (Figs. 3E, 6A, B, F, G and H) and occurs alongside Si-rich goethite, hematite and Mn-dolomite to Ca-rhodochrosite (Fig. 4). The massive pyrolusite shows a wide range of textures from tiny micrometric needles to large prismatic millimetric crystals (Figs. 3E, 6B and F). Variation of pyrolusite bonds in Raman spectra (Fig. 6D) are interpreted as replacement of

manganite (Gaudefroy, 1960; Hewett, 1972; Pasero, 2005; Post, 1999; Yoshino et al., 1993, 1992). Prismatic pyrolusite is frequently related to manganite replacement (Fleischer et al., 1962). The replacement of Mn^{2+}- or Mn^{3+}-bearing minerals by pyrolusite enhances the Jahn Teller deformation pattern by including a c-axis elongated Mn^{3+}-octahedra in the pyrolusite structure (Julien et al., 2004; Post, 1999; Post et al., 2003; Zwicker et al., 1962). These textures indicate that this mineralization stage impregnates the host rock dolostone and support that pyrolusite partly replaced manganite. Also important is that pyrolusite remains stable and does not accommodate any supplementary cation other than Mn in its structure, unlike manganite, for which substitutions are facilitated by its layer structure (Post, 1999; Post et al., 2003). Conversion from manganite to pyrolusite explains Si, Al and Ca (>2 wt.%) enrichment in pyrolusite (Tables 3 and 5). Mn-Fe oxides precipitated from a similar mineralizing fluid, although Si-rich Fe oxides formed later than pyrolusite (Fig. 7E). This means that this second ore formation stage partly reworks the early mineralization episode. Although, pyrolusite by replacement of manganite is well documented in the Bou Arfa ore, the main ore consists of open-space filling of pyrolusite (Figs. 6A and F). Botryoidal-hematite, proto-hematite and goethite formed later than Dol-2 and destabilized some dolomitic phases (Fig. 4).

5.1.3 Late stage supergene enrichment

The post-ore supergene stage is poorly expressed in the Bou Arfa ores (Fig. 4). This feature is due to the stability of the main ore-forming minerals under surface or near-surface conditions (Post, 1999), such as pyrolusite and Fe oxides. Some typical supergene minerals have unevenly precipitated as chalcophanite or hollandite-cryptomelane (Figs. 6F, 7A and B) in partial replacement of hausmannite. Chalcophanite is a common weathering product in Mn and Zn deposits (Decrée et al., 2010, 2008; Ostwald, 1992; Post, 1999), and its relation with hausmannite is due to little amounts of Zn (0.3 wt.%; Table 5). Pyrolusite is also partially destabilized and transformed into coronadite group minerals (here hollandite and cryptomelane) as it is often the case in the weathering zone of Mn deposits (Ostwald, 1992; Varentsov, 1996). Late calcite cement (Figs. 3E and F) is also associated with the Mn supergene assemblage and extensively develops in the host rock and mineralization (Fig. 4). The meteoric origin of calcite is supported by partial dedolomitisation (Fig. 3E; Ayora et al. 1998; Dewaide et al. 2014) and light isotopic values (Fig. 11).

5.2 Metallogenic model

5.2.1 Metal source(s) in seawater

All mineralization, whatever their stage, display similar geochemical patterns (Fig. 10B), close to the signal of the host rock dolostone (Figs. 10A and B). It implies that the three ore stages have a similar origin and that the later stages rework an early stock. Chalcophile (As, Zn, Pb, Cu, Ni, Co, V) and some mobile elements (Sr, Ba, Be; Table 3; Figs. 10A and B) are particularly enriched in the orebodies. However, a Principal Component Analysis (PCA) also links As, V, Mo, Co, Ni, Ba, Zn, Sr, Pb, U to the Mn orebodies, unlike immobile and lithophile, which characterize the host Sinemurian dolostone and the Pliensbachian arkoses (Fig. 12A). This indicates that the Mn ore involves external inputs of Mn and associated metals, i.e. from basement rocks. Therefore, it is likely that upward (hot?) mineralizing fluids additionally participated to the ore formation, for example by mixing with shallower oxygenated ground waters, which might explain the karst-like mineralization (Varentsov, 1996). This is materialized in Nicholson's diagnostic plots by a clear hydrothermal trend of the Bou Arfa ores (Figs. 12B; Fig. 12C). In addition, this highlights the difference between the Bou Arfa Mn ores from other carbonate-hosted Mn deposits in Morocco (Fig. 12C; Gutzmer et al. 2006; Dekoninck et al. 2016b, a, 2020).

5.2.2 Syn-sedimentary and early diagenetic (pre)concentration

The occurrence of evaporitic levels, pisoids, oncoids, bird eyes and micro-saccharoïdal dolomite (Dol-1; Fig. 3) supports a restricted lagoonal environment, part of the platform interior. This restricted lagoon is protected from open marine environments by an ooid and bioclatic sand shoal, probably forming the platform margin 4-5 km south of the Mn ore deposit of Aïn Beida, in the Jbel Bou Mokhta (Fig. 1B). These restricted lagoonal environments are particularly suitable for early dolomitization (Fig. 4; Land 1985; Jones and Renaut 1994; Machel 2004; Arenas-Abad et al. 2010). The oxygen composition of Dol-1 are higher than most common lagoonal dolomite (Blaise et al., 2014; Brigaud et al., 2018; Mauger and Compton, 2011; Ren and Jones, 2017), but they are consistent with shallow depth Mn-rich dolomite (Burns and Baker 1987; Fig. 11). Dolomite (Dol-1) is less abundant in shoal and upper slope facies outside the Bou Arfa (Jbel Bou Moktha; Figs. 1B, 3G and H).

In these shallow marine to lagoonal environments, anoxic to suboxic basins or microbial activity are the most suitable trap for Mn (Folk and Chafetz, 2000; Jones and Renaut, 1994; Mandernack et al., 1995b, 1995a; Ostwald, 1990). Microbial activity is usually observed through the coalescence of Mn-Fe-rich pisoid laminae in sedimentary Mn deposits (Groote Eylandt, Chinese, Brazil deposits; Force and Cannon 1988; Frakes and Bolton 1992; Ostwald 1992; Fan and Yang 1999; Fan et al. 1999; Biondi et al. 2020). The absence of Mn-rich or Fe-rich laminae and $\delta^{13}C$ isotopic values of Dol-1 greater than 0‰ VPDB (Fig. 11) are not consistent with Mn and Fe enrichment by bacteria-mediated organic matter degradation

(i.e., black shales; Okita et al. 1988; Polgári et al. 1991, 2012; Fan et al. 1999; Maynard 2014; Johnson et al. 2016). Alternatively, the C-O evolutionary trend shown in Figure 11 could be interpreted as resulting from fluid mixing between deep upward migrating warm basinal brines and downward infiltration of later cooler meteoric fluid. However, C-rich layers (i.e., coal, lignite) are not present in the sedimentary series. A second dolomitization episode is recorded by Dol-2, although no textural argument clearly establishes if this second event belongs to an early diagenesis or epigenesis (Fig. 5).

The high Mn contents of Dol-1 (up to 1.58 ± 0.51 wt.% MnO in Dol-1; Table 4) suggests an early Mn enrichment (Fig. 9C) under suboxic conditions with the absence Fe sulfides or Fe carbonates (Maynard 2014). Without any contribution of organic matter in the Mn fixation, an extremely high alkaline and anoxic to dysoxic environment (0-0.4 Eh) would prevail. Anoxic-suboxic events related to the closure of a narrow and shallow Bou Arfa basin (Piqué et al., 2000; Yelles-Chaouche et al., 2001) may trap the dissolved Mn^{2+} in pore waters. The porosity increased thanks to the early dolomitization and transformation of the earliest carbonates into dolomite. The high Mg:Mn ratio favors precipitation of dolomite with little amounts of Mn, the major part staying in the pore fluid (Table 2). Burial of the Sinemurian sediments would reinforce suboxic conditions that precipitate Mn^{2+} from pore waters into "reduced" Mn oxides (Mn^{2+} and Mn^{3+}), when alkaline conditions are maintained. The high As content in goethite (Table 6) is also consistent with a precipitation under alkaline and suboxic conditions (Campbell and Nordstrom, 2014; Pierce and Moore, 1982). At the same time, dolomitization continued, increasing the porosity of the host rock, and helped to accommodate CO_3^{2-} from pore waters into dolomite phase. The extensive pseudomorphosis between dolomite generations during the ore formation (Figs. 3 and 4) may have limited massive release of CO_3^{2-} in pore waters, and have prevented the formation of Mn-rich carbonates (i.e., Ca-rhodochrosite or kutnohorite; Fig. 4). Only alteration of this primary ore assemblage led to Ca-rhodochrosite (Figs. 4 and 7C; Maynard 2014; Manceau et al. 2014). Consequently, hausmannite and manganite precipitated instead of Mn carbonates. The presence of Mn-rich Fe oxides in the primary stage also indicates a local separation of Fe from Mn at macro/microscopic scale. However, the high Mn content in goethite shows that Fe and Mn probably came with the same mineralizing fluid, but have precipitated separate phases, in different proportions. It likely suggests that the mineralizing fluids carried Mn and Fe with a very low Fe/Mn ratio (Table 6; Fig. 9C).

5.2.3 Late diagenetic evolution and hydrothermal circulation during burial

The synchronous precipitation of manganite, hausmannite and barite in Mn deposits are commonly attributed to thermal conditions with temperatures much higher (250-350°C)

than at the surface (Fan et al., 1999; Gutzmer and Beukes, 1996; Hewett, 1972). Dol-2b and Dol-3 display sub-planar to saddle texture (Figs. 3C and F) due to an increase of temperature (Blaise et al., 2014; Radke and Mathis, 1980; Searl, 1989). Decrease of the $\delta^{18}O$ values and slight decrease of $\delta^{13}C$ values from Dol-1 to Dol-2 (Fig. 9) is characteristic of an isotopic re-equilibration triggered by a temperature increase (Brand and Veizer, 1981; Lee and Friedman, 1987; Nader et al., 2007, 2006; Warren, 2000). Moreover, $\delta^{18}O$ and $\delta^{13}C$ values of the saddle dolomite (Dol-3) are among the lightest (Fig. 9) and support a continuous increase in temperature along the formation of the dolomite generations, and consequently along the formation of the Bou Arfa Mn(-Fe) ores. The saddle dolomite (Dol-3b) originates from a thermal effect instead of oversaturation of Mg (Searl, 1989; Warren, 2000). The temperature allowing non-planar dolomite (Dol-2b) is close to 50°C and a temperature of 60°C to 80°C is needed for the saddle dolomite formation (Dol-3b; Radke and Mathis 1980; Machel 2000; Warren 2000). This thermal effect is also shown through the crystallography of Fe oxides (Fig. 8; Table 9). In experiments, the formation of proto-hematite occurs beyond ~140°C (Wolska and Schwertmann, 1989) and the short a axis of the goethite cell at Bou Arfa (Table 9) testifies to the higher formation temperatures (>50°C; Schwertmann et al. 1985). This interpretation is further supported by the evolutionary trend shown by the distribution of C and O isotopic data (Fig. 11) and an important change in $\delta^{13}C$ from the classical burial diagenesis in Dol 3. This involves warm basinal brines and their subsequent mixing with downward percolating cooler meteoric fluids. The E-W-trending Aïn Beida fault zone would have enhanced the widespread infiltration of meteoric fluids. These observations indicate that burial and additional hot fluids are the driver for late dolomitization (Dol-2 and Dol-3) and Fe oxide stages (Fig. 5). It is materialized by karst and vein mineralization (Fig. 6A, F, 6A, B and C) and by mineralogical transformations of the primary ore (Fig. 5). The successive dolomite generations are similar to the burial model of Cu-Co deposits described in the Central Africa Copper Belt (Dewaele et al., 2006; El Desouky et al., 2009; Hoy and Ohmoto, 1989). The formation of Mn-rich dolomite and Ca-rhodochrosite are also indicators of burial diagenesis in the Bou Arfa deposit (Fig. 4). Actually, the reductive conditions related to burial and the loss of oxygen renewal is suitable for the partial manganite degradation into Ca-rhodochrosite (Fig. 7C; Roy 2006; Johnson et al. 2016).

Consequently, the genesis of the remobilized ore (Fig. 5) might be due to (i) remobilization of the primary ore and (ii) migration of Mn by diagenetically-driven hydrothermal fluids. The Aïn Beida fault (Fig. 1B) played an important role by facilitating fracturation of the host rock and enhancing Mn-bearing fluid circulation. It is not excluded that hausmannite and manganite resulted from the transformation of former Mn oxides. Such mineral evolution is common in hypogene and metamorphic Mn deposits (Hewett 1972;

Nicholson 1992; Gutzmer et al. 1995; Post 1999). There are few petrographical arguments pleading for the presence of an early Mn carbonate precursor as formerly presented by Pouit and Jouravsky (1965).

5.2.4. The Cenozoic Atlas exhumation: supergene enrichment

Hollandite, cryptomelane and chalcophanite (Figs. 6F and G) were accompanied by dedolomitisation (Fig. 4E). These late meteoric fluids have not substantially enriched the Bou Arfa ore, except maybe for Zn that was concentrated in chalcophanite, and Sr in hollandite-cryptomelane (Table 3). The supergene origin of the Fe oxides is unlikely with their crystallographic features (Fig. 8; Table 9) and explains why these minerals have precipitated later than manganite, hausmannite and pyrolusite. This relatively poor weathering is quite contrasting with the numerous Cu-Zn-Pb-V hypogene deposits of the eastern High Atlas and Anti-Atlas, where an oxidation zone systematically occurs (Bouabdellah et al., 2012; Choulet et al., 2014; Poot et al., 2020; Rddad and Bouhlel, 2016; Verhaert et al., 2018, 2017). The weathering phase recorded in the Bou Arfa ores is probably connected to the repeated exhumation of the Atlas since late Cretaceous times (Dekoninck et al., 2020; Frizon de Lamotte et al., 2000; Froitzheim, 1984; Leprêtre et al., 2018, 2015).

5.3 Place of the Mn Bou Arfa deposit in the Mesozoic evolution of the Atlas

Without geochronological constraints, the absolute timing of the Bou Arfa Mn(-Fe) mineralization is difficult to establish, but has seemingly occurred after the deposition of the Sinemurian carbonates. Sinemurian dolostones were deposited in the context of rifting and deepening of several sedimentary basins along the Atlas belt (Frizon de Lamotte et al., 2009; Nottvedt et al., 1995; Teixell et al., 2009; White and McKenzie, 1988). This setting would explain the position of the Bou Arfa Mn deposit, as the basin could act as a threshold, given its location above a paleohigh. The strong variation in the thickness of the sedimentary series in the Bou Arfa basin indicates an important variation of the geometry and/or significant lateral variation of the sedimentary facies that would have delimited the extension of the Mn mineralization (Torres-Ruiz, 1983). This sharp transition of sedimentary facies is well demonstrated in the Jbel Bou Moktha (Fig. 1B), where the Sinemurian carbonate facies evolves from a lagoonal (dolomitic-peloidal facies) to an offshore environment (marls/limestones alternations). Transgression events during the Sinemurian interval repeatedly supplied dissolved Mn^{2+}, and when the Bou Arfa area was isolated from seawater influxes, was trapped in pore waters. The situation of the Bou Arfa deposit in a narrow basin pinched to the north by the Tendrara rift shoulder and to the south by a narrow ditch (Tamlet plain; Piqué et al. 2000; Yelles-Chaouche et al. 2001) was an efficient trap for dolomitization and Mn pre-concentration. The position of the deposit above paleohigh basement rocks and

close to a major tectonic thrust (Fig. 1B) have provided suitable conditions for brecciation and fracking enhancing diagenetically-driven hydrothermal circulation in porous Sinemurian dolostones.

The metallogenesis of the Bou Arfa ores is different from the high-grade Imini-Tasdremt Mn deposits (Figs. 12B and C). Accordingly, the Imini-Tasdremt Mn ores postdate the latest meteoric dolomite generation and do not show any Mn precursor (Dekoninck et al., 2016a) nor saddle dolomite (Force et al., 1986). Moreover, the host dolostone is intensely karstified with dissolution and collapse breccia filled by sands (Gutzmer et al., 2006) and the age of the Mn ore span over a period of ~25 Ma during the late Cretaceous (Dekoninck et al., 2020). The accepted formation model of the Imini-Tasdremt ores involves mixing of O_2-rich meteoric waters and acidic O_2-free ground waters (Gutzmer et al., 2006). For these reasons, the comparison between these two carbonate-hosted Mn deposits is unfaithful although the dolomitic trap has some similarities, i.e. the isotopic composition (Fig. 11) and Fe:Mn ratios (Fig. 9C) of the host dolostones.

5.4. Relation of the Bou Arfa Mn(-Fe) ores with Mississippi Valley Type deposits in North Africa

Mississippi Valley Type (MVT) deposits are widespread along Meso-Cenozoic shallow-water carbonate platforms forming the Atlas system (Bouabdellah and Sangster, 2016; Decrée et al., 2016). The occurrence of numerous Pb-Zn MVT and Cu mineralization in Jurassic series of the Bou Arfa region (Fig. 1; e.g., Chefchaouni et al. 1963; Verhaert et al. 2017, 2018) also supports the predominant role of dolostone in trapping various metals. The Bou Arfa deposit is comparable with major Zn-Pb MVT deposits of Morocco (Bouabdellah et al., 2015, 2012; Bouabdellah and Sangster, 2016; Jébrak et al., 1998; Rddad, 2021; Rddad et al., 2018; Rddad and Bouhlel, 2016) at several levels: (1) they are hosted in Lower to Middle Jurassic unmetamorphosed platform carbonate rocks; (2) the mineralization fills open spaces (veins, interconnected cavities, solution-collapse breccias) and replaces carbonate; (3) the mineralization is accompanied by different generations of saddle dolomite or calcite; (4) the deposits are located above basement paleohighs where Triassic to Jurassic rocks are pinched out; and (5) the ENE-WSW and E-W faults have facilitated fluid circulation in permeable rocks hosting the ore. The genesis of Pb-Zn MVT mineralization in Morocco is explained by ascending diagenetically-derived hydrothermal solutions due to compaction and/or gravity-driven systems mixing with surficial cooler fluids. The mineralizing fluids were forced to spread laterally along the porous Lower and Middle Jurassic aquifer due to Upper Jurassic cap rock (Bouabdellah and Sangster, 2016). MVT deposits are likely formed before the onset of the non-sulphide supergene ores supposed at ~20 Ma (Choulet et al., 2014;

Verhaert et al., 2017). The heat source for MVT deposits in the Atlas range may derived from the Alpine orogenesis itself that caused large-scale fluid circulation of deep-seated fluids rather than direct volcanic activities (Rddad, 2021). The High Atlas has indeed a thin lithosphere supported by a thermal anomaly since the Miocene (Leprêtre et al., 2018 and reference therein), which has provided proper thermal conditions for various mineralization types in the High Atlas. Such interpretation can be applied to the Bou Arfa Mn(-Fe) deposit.

6. CONCLUSIONS

This study emphasizes the role of dolomitization in the formation of the Bou Arfa Mn(-Fe) deposit. The accumulation of the Bou Arfa Mn ores follows a multistage genesis in close association with three dolomite events. Early diagenesis (Dol-1 and Dol-2) and epigenesis (Dol-3) are associated with the mineralization process by providing suitable conditions for Mn oxides precipitation instead of Mn carbonates. The porosity, depletion in dissolved carbonate species in pore waters and suboxic conditions are responsible for the primary hausmannite, manganite, barite and (Mn-)goethite assemblage. The subsequent burial of the host Sinemurian dolostone is clearly observed through (i) a textural evolution from non-planar (Dol-2b) to saddle dolomite (Dol-3), (ii) a decrease in the $\delta^{13}C$ and $\delta^{18}O$ isotopic values and (iii) crystallographic changes of the Fe oxides. This increase in temperature and pressure triggered mineralogical transformations of the primary manganite into massive pyrolusite with (Si-)goethite, hematite and (Mn-)dolomite to Ca-rhodochrosite, whereas hausmannite remained stable. Diagenetically-driven hydrothermal circulation, enhanced by the vicinity of the Aïn Beida fault, is responsible for the formation of deep karst and vein-type Mn and then Fe ores. A mixing fluid model is also suitable for the late evolution of the Mn mineralization. It emphasizes that goethite and some of the Mn oxides, commonly attributed to strictly supergene conditions, were formed under higher temperatures (>50°C). The supergene contribution is very low given the stability of the ore-forming minerals under supergene conditions. Weathering only proceeded through partial replacement of hausmannite (and rarely pyrolusite) into chalcophanite and coronadite group minerals.

The Bou Arfa deposit can be considered as a diagenetic deposit showing similarities with MVT deposits of North Africa, where a predominant role is played by dolomitization. In the context of global extension (opening of Tethys) forming several Jurassic basins along the High Atlas, the Bou Arfa area played differently due to local settings. This narrow basin lying above a paleohigh basement in a heavily faulted zone probably facilitated circulation of diagenetic fluids and strictly delimited the geometry of the Mn ores. Transgression-regression intervals determined the input of dissolved Mn into the basin.

Acknowledgement

We warmly thank the Caïdat of Bou Arfa and the ONHYM for giving access to outcrops and samples. We are grateful to Michel Dubois, head manager of the CGCE laboratory of the University of Lille 1 (France) for helping us in the acquisition of Raman spectra. We greatly appreciated the help of Gaëtan Rochez for taking field pictures and collecting samples. This research did not receive any specific grant from funding agencies in the public, commercial, or not-for-profit sectors. Michèle Verhaert thanks the Belgian Fund for Scientific Research (FNRS) for providing a FRIA PhD grant.

References

Arenas-Abad, C., Vázquez-Urbez, M., Pardo-Tirapu, G., Sancho-Marcén, C., 2010. Chapter 3 Fluvial and Associated Carbonate Deposits, in: Developments in Sedimentology. Elsevier, pp. 133–175. https://doi.org/10.1016/S0070-4571(09)06103-2

Ayora, C., Taberner, C., Saaltink, M.W., Carrera, J., 1998. The genesis of dedolomites: a discusion based on reactive transport modeling. Journal of Hydrology 209, 346–365. https://doi.org/10.1016/S0022-1694(98)00095-X

Biondi, J.C., Polgári, M., Gyollai, I., Fintor, K., Kovács, I., Fekete, J., Mojzsis, S.J., 2020. Biogenesis of the Neoproterozoic kremydilite manganese ores from Urucum (Brazil) – A new manganese ore type. Precambrian Research 340, 105624. https://doi.org/10.1016/j.precamres.2020.105624

Blaise, T., Barbarand, J., Kars, M., Ploquin, F., Aubourg, C., Brigaud, B., Cathelineau, M., El Albani, A., Gautheron, C., Izart, A., Janots, D., Michels, R., Pagel, M., Pozzi, J.-P., Boiron, M.-C., Landrein, P., 2014. Reconstruction of low temperature (<100 °C) burial in sedimentary basins: A comparison of geothermometer in the intracontinental Paris Basin. Marine and Petroleum Geology 53, 71–87. https://doi.org/10.1016/j.marpetgeo.2013.08.019

Bouabdellah, M., Niedermann, S., Velasco, F., 2015. The Touissit-Bou Beker Mississippi Valley-Type District of Northeastern Morocco: Relationships to the Messinian Salinity Crisis, Late Neogene-Quaternary Alkaline Magmatism, and Buoyancy-Driven Fluid Convection. Economic Geology 110, 1455–1484. https://doi.org/10.2113/econgeo.110.6.1455

Bouabdellah, M., Sangster, D.F., 2016. Geology, Geochemistry, and Current Genetic Models for Major Mississippi Valley-Type Pb–Zn Deposits of Morocco, in: Bouabdellah, M., Slack, J.F. (Eds.), Mineral Deposits of North Africa, Mineral Resource Reviews. Springer International Publishing, Cham, pp. 463–495. https://doi.org/10.1007/978-3-319-31733-5_19

Bouabdellah, M., Sangster, D.F., Leach, D.L., Brown, A.C., Johnson, C.A., Emsbo, P., 2012. Genesis of the Touissit-Bou Beker Mississippi Valley-Type District (Morocco-Algeria) and Its Relationship to the Africa-Europe Collision. Economic Geology 107, 117–146. https://doi.org/10.2113/econgeo.107.1.117

Brand, J., Veizer, J., 1980. Chemical diagenesis of a multicomponent carbonate system: trace elements. SEPM Journal of Sedimentary Research Vol. 50. https://doi.org/10.1306/212F7BB7-2B24-11D7-8648000102C1865D

Brand, U., Veizer, J., 1981. Chemical diagenesis of a multicomponent carbonate system; 2, Stable isotopes. Journal of Sedimentary Research 51, 987–997. https://doi.org/10.1306/212F7DF6-2B24-11D7-8648000102C1865D

Brigaud, B., Vincent, B., Pagel, M., Gras, A., Noret, A., Landrein, P., Huret, E., 2018. Sedimentary architecture, depositional facies and diagenetic response to intracratonic deformation and climate change inferred from outcrops for a pivotal period (Jurassic/Cretaceous boundary, Paris Basin, France). Sedimentary Geology 373, 48–76. https://doi.org/10.1016/j.sedgeo.2018.04.011

776 Burns, S.J., Baker, P.A., 1987. A geochemical study of dolomite in the Monterey Formation,
777 California. Journal of Sedimentary Research 57, 128–139.
778 https://doi.org/10.1306/212F8AC6-2B24-11D7-8648000102C1865D
779 Calvert, S.E., Pedersen, T.F., 1996. Sedimentary geochemistry of manganese; implications
780 for the environment of formation of manganiferous black shales. Economic Geology
781 91, 36–47. https://doi.org/10.2113/gsecongeo.91.1.36
782 Campbell, K.M., Nordstrom, D.K., 2014. Arsenic Speciation and Sorption in Natural
783 Environments. Reviews in Mineralogy and Geochemistry 79, 185–216.
784 https://doi.org/10.2138/rmg.2014.79.3
785 Cannon, W.F., Force, E.R., 1983. Potential for high-grade shallow-marine manganese
786 deposits in North America, in: Cameron Volume on Unconventional Mineral Deposits.
787 American Institute of Mining, Metallurgical and Petroleum Engineers, New York, NY,
788 pp. 175–189.
789 Chefchaouni, Y.C., Diouri, M., Choubert, G., 1963. Carte géologique de la France à 1/50
790 000, 341, Gérardmer. Notes et mémoires du Service géologique du Maroc.
791 Choubert, G., Faure-Muret, A., 1973. The Precambrian iron and manganese deposits of the
792 Anti-Atlas, in: Genesis of Precambrian Iron and Manganese Deposits. Presented at
793 the Unesco Earth Sciences Symposium, Kiev, pp. 115–124.
794 Choubert, G., Faure-Muret, A., 1962. Evolution du domaine atlasique marocain depuis les
795 temps paléozoïques, in: Livre à La Mémoire Du Professeur Paul Fallot, Mémoire Hors
796 Série. Société Géologique de France, Paris, pp. 447–527.
797 Choulet, F., Charles, N., Barbanson, L., Branquet, Y., Sizaret, S., Ennaciri, A., Badra, L.,
798 Chen, Y., 2014. Non-sulfide zinc deposits of the Moroccan High Atlas: Multi-scale
799 characterization and origin. Ore Geology Reviews 56, 115–140.
800 https://doi.org/10.1016/j.oregeorev.2013.08.015
801 Cornell, R.M., Schwertmann, U., 2003. The Iron Oxides: Structure, Properties, Reactions,
802 Occurences and Uses, 1st ed. Wiley. https://doi.org/10.1002/3527602097
803 de Wolff, P.M.D., 1959. Interpretation of some γ-MnO2 diffraction patterns. Acta
804 Crystallographica 12, 341–345. https://doi.org/10.1107/S0365110X59001001
805 Decrée, S., De Putter, T., Yans, J., Moussi, B., Recourt, P., Jamoussi, F., Bruyère, D.,
806 Dupuis, C., 2008. Iron mineralisation in Mio-Pliocene sediments of the Tamra iron
807 mine (Nefza mining district, Tunisia): Mixed influence of pedogenesis and
808 hydrothermal alteration. Ore Geology Reviews 33, 397–410.
809 https://doi.org/10.1016/j.oregeorev.2007.02.001
810 Decrée, S., Marignac, C., Abidi, R., Jemmali, N., Deloule, E., Souissi, F., 2016.
811 Tectonomagmatic Context of Sedex Pb–Zn and Polymetallic Ore Deposits of the
812 Nappe Zone Northern Tunisia, and Comparisons with MVT Deposits in the Region, in:
813 Bouabdellah, M., Slack, J.F. (Eds.), Mineral Deposits of North Africa. Springer
814 International Publishing, Cham, pp. 497–525. https://doi.org/10.1007/978-3-319-
815 31733-5_20
816 Decrée, S., Ruffet, G., Putter, T.D., Baele, J.-M., Recourt, P., Jamoussi, F., Yans, J., 2010.
817 Mn oxides as efficient traps for metal pollutants in a polyphase low-temperature
818 Pliocene environment: A case study in the Tamra iron mine, Nefza mining district,
819 Tunisia. Journal of African Earth Sciences 57, 249–261.
820 https://doi.org/10.1016/j.jafrearsci.2009.08.005
821 Dekoninck, A., Bernard, A., Barbarand, J., Saint-Bezar, B., Missenard, Y., Lepretre, R.,
822 Saddiqi, O., Yans, J., 2016a. Detailed mineralogy and petrology of manganese
823 oxyhydroxide deposits of the Imini district (Morocco). Mineralium Deposita 51, 13–23.
824 https://doi.org/10.1007/s00126-015-0590-3
825 Dekoninck, A., Leprêtre, R., Saddiqi, O., Barbarand, J., Yans, J., 2016b. The high-grade
826 Imini manganese district—karst-hosted deposits of mn oxides and oxyhydroxides, in:
827 Bouabdellah, M., Slack, J.F. (Eds.), Mineral Deposits of North Africa. Springer
828 International Publishing, Cham, pp. 575–594.
829 Dekoninck, A., Ruffet, G., Missenard, Y., Parizot, O., Magoua, M., Mouttaqi, A., Rochez,
830 Gaëtan, Yans, J., 2020. Multistage genesis of the late Cretaceous manganese karst-

hosted Tasdremt deposit (High Atlas, Morocco). Mineralium Deposita. https://doi.org/10.1007/s00126-020-01017-0

Dewaele, S., Muchez, Ph., Vets, J., Fernandez-Alonzo, M., Tack, L., 2006. Multiphase origin of the Cu–Co ore deposits in the western part of the Lufilian fold-and-thrust belt, Katanga (Democratic Republic of Congo). Journal of African Earth Sciences 46, 455–469. https://doi.org/10.1016/j.jafrearsci.2006.08.002

Dewaide, L., Baele, J.-M., Collon-Drouaillet, P., Quinif, Y., Rochez, G., Vandycke, S., Hallet, V., 2014. Karstification in dolomitized Waulsortian mudmounds (Belgium). Geologica Belgica 17, 43–51.

du Dresnay, R., 1965. Notice géologique sur la région de Bou-Arfa – Colloque sur les gîtes stratiformes de plomb, zinc et manganèse du Maroc (2 mai - 14 mai 1962). Notes et Mémoires du Service Géologique du Maroc 181, 107–112.

El Desouky, H.A., Muchez, P., Cailteux, J., 2009. Two Cu–Co sulfide phases and contrasting fluid systems in the Katanga Copperbelt, Democratic Republic of Congo. Ore Geology Reviews 36, 315–332. https://doi.org/10.1016/j.oregeorev.2009.07.003

Fan, D., Yang, P., 1999. Introduction to and classification of manganese deposits of China. Ore Geology Reviews 15, 1–13. https://doi.org/10.1016/S0169-1368(99)00011-6

Fan, D., Ye, J., Li, J., 1999. Geology, mineralogy, and geochemistry of the Middle Proterozoic Wafangzi ferromanganese deposit, Liaoning Province, China. Ore Geology Reviews 15, 31–53. https://doi.org/10.1016/S0169-1368(99)00013-X

Fleet, A.J., 1983. Hydrothermal and Hydrogenous Ferro-Manganese Deposits: Do They form a Continuum? The Rare Earth Element Evidence, in: Rona, P.A., Boström, K., Laubier, L., Smith, K.L. (Eds.), Hydrothermal Processes at Seafloor Spreading Centers. Springer US, Boston, MA, pp. 535–555. https://doi.org/10.1007/978-1-4899-0402-7_23

Fleischer, M., Richmond, W.E., Evans, H.T., 1962. Studies of manganese oxides. 5. Ramsdellite MnO2, an orthorhombic dimorph of pyrolusite. American Mineralogist 47, 47–58.

Folk, R.L., Chafetz, H.S., 2000. Bacterially Induced Microscale and Nanoscale Carbonate Precipitates, in: Riding, R.E., Awramik, S.M. (Eds.), Microbial Sediments. Springer, Berlin, Heidelberg, pp. 40–49. https://doi.org/10.1007/978-3-662-04036-2_6

Force, E.R., Back, W., Spiker, E.C., Knauth, L.P., 1986. A ground-water mixing model for the origin of the Imini manganese deposit (Cretaceous) of Morocco. Economic Geology 81, 65–79. https://doi.org/10.2113/gsecongeo.81.1.65

Force, E.R., Cannon, W.F., 1988. Depositional model for shallow-marine manganese deposits around black shale basins. Economic Geology 83, 93–117. https://doi.org/10.2113/gsecongeo.83.1.93

Force, E.R., Maynard, J.B., 1991. Manganese: Syngenetic deposits on the margins of anoxic basins, in: Sedimentary and Diagenetic Mineral Deposits: A Basin Analysis Approach to Exploration. Society of Economic Geologists, Littleton, Colorado, pp. 147–159.

Frakes, L., Bolton, B.R., 1992. Effects of ocean chemistry, sea level, and climate on the formation of primary sedimentary manganese ore deposits. Economic Geology 87, 1207–1217. https://doi.org/10.2113/gsecongeo.87.5.1207

Frizon de Lamotte, D., Leturmy, P., Missenard, Y., Khomsi, S., Ruiz, G., Saddiqi, O., Guillocheau, F., Michard, A., 2009. Mesozoic and Cenozoic vertical movements in the Atlas system (Algeria, Morocco, Tunisia): An overview. Tectonophysics 475, 9–28. https://doi.org/10.1016/j.tecto.2008.10.024

Frizon de Lamotte, D., Saint Bezar, B., Bracène, R., Mercier, E., 2000. The two main steps of the Atlas building and geodynamics of the western Mediterranean. Tectonics 19, 740–761. https://doi.org/10.1029/2000TC900003

Froitzheim, N., 1984. Late Cretaceous vertical tectonics in the High Atlas SW of Marrakech/Morocco - Reconstruction of tectonic movements in an early stage of the High Atlas orogenesis. Neu Jb Paläont Mh 463–471.

Fu, Q., Qing, H., Bergman, K.M., 2006. Early dolomitization and recrystallization of carbonate in an evaporite basin: the Middle Devonian Ratner laminite in southern

886 Saskatchewan, Canada. Journal of the Geological Society 163, 937–948.
887 https://doi.org/10.1144/0016-76492005-088
888 Gao, T., Fjellvåg, H., Norby, P., 2009. A comparison study on Raman scattering properties of
889 α- and β-MnO2. Analytica Chimica Acta 648, 235–239.
890 https://doi.org/10.1016/j.aca.2009.06.059
891 Gasparrinia, M., Bakker, R.J., Bechstddt, Th., Boni, M., 2003. Hot dolomites in a Variscan
892 foreland belt: hydrothermal flow in the Cantabrian Zone (NW Spain). Journal of
893 Geochemical Exploration, Proceedings of Geofluids IV 78–79, 501–507.
894 https://doi.org/10.1016/S0375-6742(03)00115-8
895 Gaudefroy, G., 1960. Caractères distinctifs de la pyrolusite - ex manganite (application au
896 minerai de l'Imini). Notes du Service Géologique Marocain 19, 77–86.
897 Glasby, G.P., 2006. Manganese: Predominant Role of Nodules and Crusts, in: Schulz, H.D.,
898 Zabel, M. (Eds.), Marine Geochemistry. Springer-Verlag, Berlin/Heidelberg, pp. 371–
899 427. https://doi.org/10.1007/3-540-32144-6_11
900 Gouiza, M., Charton, R., Bertotti, G., Andriessen, P., Storms, J.E.A., 2017. Post-Variscan
901 evolution of the Anti-Atlas belt of Morocco constrained from low-temperature
902 geochronology. International Journal of Earth Sciences 106, 593–616.
903 https://doi.org/10.1007/s00531-016-1325-0
904 Gualtieri, A.F., Venturelli, P., 1999. In situ study of the goethite-hematite phase
905 transformation by real time synchrotron powder diffraction. American Mineralogist 84,
906 895–904. https://doi.org/10.2138/am-1999-5-624
907 Gutzmer, J., Beukes, N.J., 1996. Mineral paragenesis of the Kalahari managanese field,
908 South Africa. Ore Geology Reviews 11, 405–428. https://doi.org/10.1016/S0169-
909 1368(96)00011-X
910 Gutzmer, J., Beukes, N.J., Kleyenstuber, A.S.E., Burger, A.M., 1995. Magnetic hausmannite
911 from hydrothermally altered manganese ore in the Palaeoproterozoic Kalahari
912 manganese deposit, Transvaal Supergroup, South Africa. Mineralogical Magazine 59,
913 703–716. https://doi.org/10.1180/minmag.1995.059.397.12
914 Gutzmer, J., Beukes, N.J., Rhalmi, M., Mukhopadhyay, J., 2006. Cretaceous karstic cave-fill
915 manganese-lead-barium deposits of Imini, Morocco. Economic Geology 101, 385–
916 405. https://doi.org/10.2113/gsecongeo.101.2.385
917 Hewett, D.F., 1972. Manganite, hausmannite, braunite: features, modes of origin. Economic
918 Geology 67, 83–102. https://doi.org/10.2113/gsecongeo.67.1.83
919 Hoy, L.D., Ohmoto, H., 1989. Constraints for the genesis of redbed associated stratiform Cu
920 deposits from sulphur and carbon mass balance relations, in: Boyle, R.W., Brown,
921 A.C., Jefferson, C.W., Jowett, E.C., Kirkham, R.V. (Eds.), Sediment-Hosted Stratiform
922 Copper Deposits. St. John's, pp. 135–149.
923 Jébrak, M., Marcoux, É., Nasloubi, M., Zaharaoui, M., 1998. From sandstone- to carbonate-
924 hosted stratabound deposits: an isotope study of galena in the Upper-Moulouya
925 District (Morocco). Mineral. Deposita 33, 406–415.
926 https://doi.org/10.1007/s001260050158
927 Johnson, J.E., Webb, S.M., Ma, C., Fischer, W.W., 2016. Manganese mineralogy and
928 diagenesis in the sedimentary rock record. Geochimica et Cosmochimica Acta 173,
929 210–231. https://doi.org/10.1016/j.gca.2015.10.027
930 Jones, B., Renaut, R.W., 1994. Crystal fabrics and microbiota in large pisoliths from Laguna
931 Pastos Grandes, Bolivia. Sedimentology 41, 1171–1202.
932 https://doi.org/10.1111/j.1365-3091.1994.tb01448.x
933 Julien, C., Massot, M., Rangan, S., Lemal, M., Guyomard, D., 2002. Study of structural
934 defects in γ-MnO2 by Raman spectroscopy. Journal of Raman Spectroscopy 33,
935 223–228. https://doi.org/10.1002/jrs.838
936 Julien, C.M., Massot, M., Poinsignon, C., 2004. Lattice vibrations of manganese oxides: Part
937 I. Periodic structures. Spectrochimica Acta Part A: Molecular and Biomolecular
938 Spectroscopy 60, 689–700. https://doi.org/10.1016/S1386-1425(03)00279-8

939 Kuleshov, V., 2016. Isotope geochemistry: the origin and formation of manganese rocks and
940 ores. Elsevier, Amsterdam Boston Heidelberg London New York Oxford Paris San
941 Diego San Francisco Singapore Sydney Tokyo.
942 Kuleshov, V.N., 2011. Manganese deposits: Communication 1. Genetic models of
943 manganese ore formation. Lithology and Mineral Resources 46, 473–493.
944 https://doi.org/10.1134/S0024490211050038
945 Lafforgue, L., 2016. Place de la minéralisation de manganèse de Bouarfa dans l'évolution
946 méso-cénozoique de l'oriental marocain (PhD). Université Paris Sud, Paris.
947 Land, L.S., 1985. The Origin of Massive Dolomite. Journal of Geological Education 33, 112–
948 125. https://doi.org/10.5408/0022-1368-33.2.112
949 Langford, J.I., Wilson, A.J.C., 1978. Scherrer after sixty years: A survey and some new
950 results in the determination of crystallite size. J Appl Cryst 11, 102–113.
951 https://doi.org/10.1107/S0021889878012844
952 Laznicka, P., 1992. Manganese deposits in the global lithogenetic system: Quantitative
953 approach. Ore Geology Reviews 7, 279–356. https://doi.org/10.1016/0169-
954 1368(92)90013-B
955 Lee, Y.I., Friedman, G.M., 1987. Deep-burial dolomitization in the Ordovician Ellenburger
956 Group carbonates, West Texas and southeastern New Mexico. Journal of
957 Sedimentary Research 57, 544–557. https://doi.org/10.1306/212F8B8E-2B24-11D7-
958 8648000102C1865D
959 Leprêtre, R., Missenard, Y., Barbarand, J., Gautheron, C., Jouvie, I., Saddiqi, O., 2018.
960 Polyphased inversions of an intracontinental rift: case study of the Marrakech High
961 Atlas, Morocco. Tectonics 37, 818–841. https://doi.org/10.1002/2017TC004693
962 Leprêtre, R., Missenard, Y., Saint-Bezar, B., Barbarand, J., Delpech, G., Yans, J.,
963 Dekoninck, A., Saddiqi, O., 2015. The three main steps of the Marrakech High Atlas
964 building in Morocco: Structural evidences from the southern foreland, Imini area.
965 Journal of African Earth Sciences 109, 177–194.
966 https://doi.org/10.1016/j.jafrearsci.2015.05.013
967 Lima-de-Faria, J., 1963. Dehydration of goethite and diaspore. Zeitschrift für Kristallographie
968 - Crystalline Materials 119, 176–203. https://doi.org/10.1524/zkri.1963.119.3-4.176
969 Machel, H.G., 2004. Concepts and models of dolomitization: a critical reappraisal. Geological
970 Society, London, Special Publications 235, 7–63.
971 https://doi.org/10.1144/GSL.SP.2004.235.01.02
972 Machel, H.G., 2000. Application of Cathodoluminescence to Carbonate Diagenesis, in:
973 Pagel, M., Barbin, V., Blanc, P., Ohnenstetter, D. (Eds.), Cathodoluminescence in
974 Geosciences. Springer Berlin Heidelberg, Berlin, Heidelberg, pp. 271–301.
975 https://doi.org/10.1007/978-3-662-04086-7_11
976 Manceau, A., Lanson, M., Takahashi, Y., 2014. Mineralogy and crystal chemistry of Mn, Fe,
977 Co, Ni, and Cu in a deep-sea Pacific polymetallic nodule. American Mineralogist 99,
978 2068–2083. https://doi.org/10.2138/am-2014-4742
979 Mandernack, K.W., Fogel, M.L., Tebo, B.M., Usui, A., 1995a. Oxygen isotope analyses of
980 chemically and microbially produced manganese oxides and manganates.
981 Geochimica et Cosmochimica Acta 59, 4409–4425. https://doi.org/10.1016/0016-
982 7037(95)00299-F
983 Mandernack, K.W., Post, J., Tebo, B.M., 1995b. Manganese mineral formation by bacterial
984 spores of the marine Bacillus, strain SG-1: Evidence for the direct oxidation of Mn(II)
985 to Mn(IV). Geochimica et Cosmochimica Acta 59, 4393–4408.
986 https://doi.org/10.1016/0016-7037(95)00298-E
987 Mattauer, M., Tapponnier, P., Proust, F., 1977. Sur les mecanismes de formation des
988 chaines intracontinentales; l'exemple des chaines atlasiques du Maroc. Bulletin de la
989 Société Géologique de France S7-XIX, 521–526.
990 https://doi.org/10.2113/gssgfbull.S7-XIX.3.521
991 Mauger, C.L., Compton, J.S., 2011. Formation of modern dolomite in hypersaline pans of the
992 Western Cape, South Africa. Sedimentology 58, 1678–1692.
993 https://doi.org/10.1111/j.1365-3091.2011.01229.x

Maynard, J.B., 2014. Manganiferous sediments, rocks, and ores, in: Treatise on Geochemistry. Elsevier, pp. 327–349.

Maynard, J.B., 2010. The chemistry of manganese ores through time: a signal of increasing diversity of earth-surface environments. Economic Geology 105, 535–552. https://doi.org/10.2113/gsecongeo.105.3.535

Meister, P., Reyes, C., 2019. The Carbon-Isotope Record of the Sub-Seafloor Biosphere. Geosciences 9, 507. https://doi.org/10.3390/geosciences9120507

Michard, A., Raddi, Y., 2011. Le manganèse de Bou-Arfa (Haut Atlas oriental), in: Mouttaqi, A., Rjimati, E.C., Maacha, L., Michard, André, Soulaimani, A., Ibouh, H. (Eds.), Les Principales Mines Du Maroc, Notes et Mémoires Du Service Géologique. Notes et mémoires du service géologique, Rabat, pp. 305–308.

Missenard, Y., Saddiqi, O., Barbarand, J., Leturmy, P., Ruiz, G., El Haimer, F.-Z., Frizon de Lamotte, D., 2008. Cenozoic denudation in the Marrakech High Atlas, Morocco: insight from apatite fission-track thermochronology. Terra Nova 20, 221–228. https://doi.org/10.1111/j.1365-3121.2008.00810.x

Missenard, Y., Zeyen, H., Frizon de Lamotte, D., Leturmy, P., Petit, C., Sébrier, M., Saddiqi, O., 2006. Crustal versus asthenospheric origin of relief of the Atlas Mountains of Morocco. Journal of Geophysical Research: Solid Earth 111, n/a-n/a. https://doi.org/10.1029/2005JB003708

Montanez, I.P., Read, J.F., 1992. Fluid-rock interaction history during stabilization of early dolomites, upper Knox Group (Lower Ordovician), U.S. Appalachians. Journal of Sedimentary Research 62, 753–778. https://doi.org/10.1306/D42679D3-2B26-11D7-8648000102C1865D

Mouttaqi, A., Rjimati, E.C., Maacha, L., Michard, A., Soulaimani, A., Ibouh, H., 2011. Les principales mines du Maroc, Editions du Service Géologique du Maroc. ed, New geological and mining guidebooks of Morocco. Ministère de l'Energie, des Mines, de l'Eau et de l'Environnement, Rabat.

Nader, F.H., Swennen, R., Ellam, R.M., 2006. Petrographic and geochemical study of Jurassic dolostones from Lebanon: Evidence for superimposed diagenetic events. Journal of Geochemical Exploration, GEOFLUIDS V: 5th International Conference on Fluid Evolution, Migration and Interaction in Sedimentary Basins and Orogenic Belts 89, 288–292. https://doi.org/10.1016/j.gexplo.2005.11.003

Nader, F.H., Swennen, R., Ellam, R.M., Immenhauser, A., 2007. Field geometry, petrography and geochemistry of a dolomitization front (Late Jurassic, central Lebanon). Sedimentology 54, 1093–1120. https://doi.org/10.1111/j.1365-3091.2007.00874.x

Nicholson, K., 1992. Contrasting mineralogical-geochemical signatures of manganese oxides; guides to metallogenesis. Economic Geology 87, 1253–1264. https://doi.org/10.2113/gsecongeo.87.5.1253

Nottvedt, A., Gabrielsen, R.H., Steel, R.J., 1995. Tectonostratigraphy and sedimentary architecture of rift basins, with reference to the northern North Sea. Marine and Petroleum Geology, Integrated Basin Studies 12, 881–901. https://doi.org/10.1016/0264-8172(95)98853-W

Okita, P.M., Maynard, J.B., Spiker, E.C., Force, E.R., 1988. Isotopic evidence for organic matter oxidation by manganese reduction in the formation of stratiform manganese carbonate ore. Geochimica et Cosmochimica Acta 52, 2679–2685. https://doi.org/10.1016/0016-7037(88)90036-1

Ostwald, J., 1992. Genesis and paragenesis of the tetravalent manganese oxides of the Australian continent. Economic Geology 87, 1237–1252. https://doi.org/10.2113/gsecongeo.87.5.1237

Ostwald, J., 1990. The biogeochemical origin of the Groote Eylandt manganese oxide pisoliths and ooliths, northern Australia. Ore Geology Reviews, Palynology of ore deposits 5, 469–490. https://doi.org/10.1016/0169-1368(90)90048-R

Pasero, M., 2005. A Short Outline of the Tunnel Oxides. Reviews in Mineralogy and Geochemistry 57, 291–305. https://doi.org/10.2138/rmg.2005.57.9

Pierce, M.L., Moore, C.B., 1982. Adsorption of arsenite and arsenate on amorphous iron hydroxide. Water Research 16, 1247–1253. https://doi.org/10.1016/0043-1354(82)90143-9

Piqué, A., Charroud, M., Laville, E., Ait Brahim, L., Amrhar, M., 2000. The Tethys southern margin in Morocco; Mesozoic and Caenozoic evolution of the Atlas domain, in: Crasquin-Soleau, S., Barrier, E. (Eds.), New Data on Peri-Tethyan Sedimentary Basins. Publications scientifiques du Muséum, Paris, pp. 93–106.

Polgári, M., Hein, J.R., Vigh, T., Szabó-Drubina, M., Fórizs, I., Bíró, L., Müller, A., Tóth, A.L., 2012. Microbial processes and the origin of the Úrkút manganese deposit, Hungary. Ore Geology Reviews 47, 87–109. https://doi.org/10.1016/j.oregeorev.2011.10.001

Polgári, M., Okita, P.M., Hein, J.R., 1991. Stable Isotope evidence for the origin of the Urkut Manganese ore deposit, Hungary. SEPM Journal of Sedimentary Research 61. https://doi.org/10.1306/D426771C-2B26-11D7-8648000102C1865D

Pomiès, M.P., Morin, G., Vignaud, C., 1998. XRD study of the goethite-hematite transformation: Application to the identification of heated prehistoric pigments. European Journal of Solid State and Inorganic Chemistry 35, 9–25. https://doi.org/10.1016/S0992-4361(98)80011-8

Poot, J., Verhaert, M., Dekoninck, A., Oummouch, A., El Basbas, A., Maacha, L., Yans, J., 2020. Characterization of Weathering Processes of the Giant Copper Deposit of Tizert (Igherm Inlier, Anti-Atlas, Morocco). Minerals 10, 620. https://doi.org/10.3390/min10070620

Post, J.E., 1999. Manganese oxide minerals: crystal structures and economic and environmental significance. Proceedings of the National Academy of Sciences 96, 3447–3454. https://doi.org/10.1073/pnas.96.7.3447

Post, J.E., Heaney, P.J., Hanson, J., 2003. Synchrotron X-ray diffraction study of the structure and dehydration behavior of todorokite. American Mineralogist 88, 142–150. https://doi.org/10.2138/am-2003-0117

Pouit, G., 1980. Manganèse. Notes et Mémoires du Service Géologique du Maroc, Rabat 13, 61–67.

Pouit, G., 1964. Les gîtes de manganèse marocains encaissés dans les Formations carbonatées : éléments pour une synthèse. Chronique des Mines et de la Recherche Minière 371–380.

Pouit, G., Jouravsky, G., 1965. Les minéralisations manganésifères de la région de Bou-Arfa - Colloque sur les gites stratiformes de plomb, zinc, et manganèse du Maroc. Notes et Mémoires du Service Géologique du Maroc 181, 113–131.

Radke, B.M., Mathis, R.L., 1980. On the formation and occurrence of saddle dolomite. Journal of Sedimentary Research 50, 1149–1168. https://doi.org/10.1306/212F7B9E-2B24-11D7-8648000102C1865D

Rddad, L., 2021. The genesis of the Jurassic-hosted Mississippi Valley-type Pb-Zn ore deposit, Tigrinine-Taabast district (Central High Atlas, Morocco): Insights from fluid inclusion and C-O-S-Pb isotope studies. Journal of African Earth Sciences 174, 104071. https://doi.org/10.1016/j.jafrearsci.2020.104071

Rddad, L., Bouhlel, S., 2016. The Bou Dahar Jurassic carbonate-hosted Pb–Zn–Ba deposits (Oriental High Atlas, Morocco): Fluid-inclusion and C–O–S–Pb isotope studies. Ore Geology Reviews 72, 1072–1087. https://doi.org/10.1016/j.oregeorev.2015.08.011

Rddad, L., Mouguina, E.M., Muchez, P., Darling, R.S., 2018. The genesis of the Ali Ou Daoud Jurassic carbonate Zn-Pb Mississippi Valley-type deposit, Moroccan central High Atlas: Constraints from bulk stable C-O-S, in situ radiogenic Pb isotopes, and fluid inclusion studies. Ore Geology Reviews 99, 365–379. https://doi.org/10.1016/j.oregeorev.2018.06.020

Ren, M., Jones, B., 2017. Spatial variations in the stoichiometry and geochemistry of Miocene dolomite from Grand Cayman: Implications for the origin of island dolostone. Sedimentary Geology 348, 69–93. https://doi.org/10.1016/j.sedgeo.2016.12.001

Rendon, J.L., Cornejo, J., de Arambarri, P., 1983. Grinding-induced effects on goethite (α-FeOOH). Journal of Colloid and Interface Science 94, 546–551. https://doi.org/10.1016/0021-9797(83)90294-1

Roy, S., 2006. Sedimentary manganese metallogenesis in response to the evolution of the Earth system. Earth-Science Reviews 77, 273–305. https://doi.org/10.1016/j.earscirev.2006.03.004

Salahane, A., 1978. Etude géologique et métallogénique du gisement cuprifère du Jbel Klakh Haut Atlas oriental (Maroc): Contribution à la métallogénie paléokarstique. Notes et Mémoires du Service Géologique du Maroc 40, 147–237.

Scherrer, P., 1918. Estimation of the size and internal structure of colloidal particles by means of röntgen. Nachrichten von der Gesellschaft der Wissenschaftenzu Göttingen Mathematisch-Physikalische Klasse, 2, 96–100.

Schwertmann, U., Cambier, P., Murad, E., 1985. Properties of Goethites of Varying Crystallinity. Clays Clay Miner. 33, 369–378. https://doi.org/10.1346/CCMN.1985.0330501

Searl, A., 1989. Saddle dolomite: a new view of its nature and origin. Mineralogical Magazine 53, 547–555. https://doi.org/10.1180/minmag.1989.053.373.05

Searl, A., Fallick, A.E., 1990. Dinantian dolomites from East Fife: hydrothermal overprinting of early mixing-zone stable isotopic and Fe/Mn compositions. Journal of the Geological Society 147, 623–638. https://doi.org/10.1144/gsjgs.147.4.0623

Seber, D., Barazangi, M., Tadili, B.A., Ramdani, M., Ibenbrahim, A., Ben Sari, D., 1996. Three-dimensional upper mantle structure beneath the intraplate Atlas and interplate Rif mountains of Morocco. Journal of Geophysical Research: Solid Earth 101, 3125–3138. https://doi.org/10.1029/95JB03112

Teixell, A., Bertotti, G., de Lamotte, D.F., Charroud, M., 2009. The geology of vertical movements of the lithosphere: An overview. Tectonophysics 475, 1–8. https://doi.org/10.1016/j.tecto.2009.08.018

Torres-Ruiz, J., 1983. Genesis and evolution of the Marquesado and adjacent iron ore deposits, Granada, Spain. Economic Geology 78, 1657–1673. https://doi.org/10.2113/gsecongeo.78.8.1657

Varentsov, I.M., 1996. Manganese ores of supergene zone: Geochemistry of formation, Solid Earth Sciences Library. Springer Netherlands, Dordrecht.

Verhaert, M., Bernard, A., Dekoninck, A., Lafforgue, L., Saddiqi, O., Yans, J., 2017. Mineralogical and geochemical characterization of supergene Cu–Pb–Zn–V ores in the Oriental High Atlas, Morocco. Mineralium Deposita. https://doi.org/10.1007/s00126-017-0753-5

Verhaert, M., Bernard, A., Saddiqi, O., Dekoninck, A., Essalhi, M., Yans, J., 2018. Mineralogy and Genesis of the Polymetallic and Polyphased Low Grade Fe-Mn-Cu Ore of Jbel Rhals Deposit (Eastern High Atlas, Morocco). Minerals 8, 39. https://doi.org/10.3390/min8020039

Walter, D., Buxbaum, G., Laqua, W., 2001. The Mechanism of the Thermal Transformation From Goethite to Hematite. Journal of Thermal Analysis and Calorimetry 63, 733–748. https://doi.org/10.1023/A:1010187921227

Wang, X., Müller, W.E.G., 2009. Marine biominerals: perspectives and challenges for polymetallic nodules and crusts. Trends in Biotechnology 27, 375–383. https://doi.org/10.1016/j.tibtech.2009.03.004

Warren, J., 2000. Dolomite: occurrence, evolution and economically important associations. Earth-Science Reviews 52, 1–81. https://doi.org/10.1016/S0012-8252(00)00022-2

White, N., McKenzie, D., 1988. Formation of the steer's head geometry of sedimentary basins by differential stretching of the crust and mantle. Geology 16, 250–253. https://doi.org/10.1130/0091-7613(1988)016<0250:FOTSSH>2.3.CO;2

Wolska, E., Schwertmann, U., 1989. Nonstoichiometric structures during dehydroxylation of goethite. Zeitschrift für Kristallographie - Crystalline Materials 189, 223–237. https://doi.org/10.1524/zkri.1989.189.3-4.223

Wolska, E., Szajda, W., 1988. The effect of cationic and anionic substitution on the α-(Al, Fe)2O3 lattice parameters. Solid State Ionics 28–30, 1320–1323. https://doi.org/10.1016/0167-2738(88)90379-7

Yelles-Chaouche, A.K., Ait Ouali, R., Bracene, R., Derder, M.E.M., Djellit, H., 2001. Chronologie de l'ouverture du bassin des Ksour (Atlas Saharien, Algerie) au debut du Mesozoique. Bulletin de la Société Géologique de France 172, 285–293. https://doi.org/10.2113/172.3.285

Yoshino, T., Miura, H., Hariya, Y., 1993. Crystal structure of orthorhombic pyrolusite from Imini mine, in: Ishihara, S., Urabe, T., Ohmoto, H. (Eds.), Mineral Resources Symposia. Society of Resource Geologists of Japan, Tokyo, pp. 62–65.

Yoshino, T., Miura, H., Hariya, Y., 1992. Crystal structure of orthorhombic pyrolusite, in: Abstract Book. Presented at the International Geological Congress, Kyoto, p. 216.

Zenger, D.H., Dunham, J.B., Ethington, R.L. (Eds.), 1980. Concepts and Models of Dolomitization. SEPM (Society for Sedimentary Geology). https://doi.org/10.2110/pec.80.28

Zwicker, W.K., Groeneveld-Meijer, W.O.J., Jaffe, H.W., 1962. Nsutite - a widespread manganese oxide mineral. American Mineralogist 47, 618–623.

Figures

Fig. 1 (color). A. Simplified structural map of Morocco showing the location of Mn mineralization. MA= Middle Atlas, EHA=Eastern High Atlas, HA= High Atlas, WHA=Western High Atlas, SAF=South Atlas Front, NAF=North Atlas Front. **B**. Local geological map of the Bou Arfa cliff and the Mn mineralization (modified after Pouit and Jouravsky 1965). H1-4=Hamaraouet, HB=Hamarouet and Aïn Beida, 63= Gallery 63.

Fig. 2 (black and white). Stratigraphic column of the Tamlet area (left) and in the Hamaraouet sector (right).

Fig. 3 (color). Petrographic views of carbonate generations in the host rock. **A.** CL view of a sandstone level at the base of the UCU cemented by Dol-1a (sample J2-2). **B.** Oolith replaced by Dol-1a and cemented by Dol-1b under CL at the bottom of the UCU. **C.** Successive generations of dolomite crystals filling fractures and void in H2 (sample H2 – Dol – Min). **D.** Bird eyes facies in the UCU dolostone at Hamaraouet (H1) crisscrossed by several calcite veins. **E.** Dedolomitization of Dol-2A in the Mn ore at Hamaraouet (H3) with pyrolusite crystals. **F.** Late calcite filling void at Hamaraouet (sample H2-Br-Dol). **G.** Early dolomite generation with ferrous (Cal-1a) and non-ferrous (Cal-1b) calcites in the UCU of the Jbel Bou Moktha under PPL prepared with a mix of alizarine-red and K-ferricyanide. **H.** Late calcite generations in the UCU of Jbel Bou Moktha under CL. Dol=dolomite, Py=pyrolusite, Ca=calcite.

Fig. 4 (color). Tentative paragenetic sequence of the Bou Arfa deposit. Schematic petrographic reconstruction of dolomite generations is given for cement and veins (see Table 6 for key features of dolomite generations).

Fig. 5 (color). Field observations of the Mn and Fe ores. See location on Fig. 1B. **A.** Galleries in the Hamaraouet area (H1) in the Upper "Chocolate" Unit. **B.** View of the Aïn Beida mining site and the Bou Arfa cliff. **C.** Stratabound orebody in gallery 63. **D.** Stockwork in the host UCU dolostone between Aïn Beida and Hamaraouet (HB). **E.** Mn and Fe oxides in the Hamaraouet area (H1). **F.** Massive goethite vein in the Hamaraouet area (H3). **G.** Fe oxide vein crossing the stratabound Mn ore in gallery 63. **H.** Stockwork of pyrolusite in the UCU in Hamaraouet (H3).

Fig. 6 (color). Petrographic views of main mineralization types. **A.** Cluster mineralization showing pyrolusite veins crossing early dolomite generation (Dol-1 and 2) filled by calcite under SEM-BSE view at Hamaraouet. **B.** Disseminated bipyramidal pyrolusite growing onto altered Dol-2B and cemented by coarse Dol-3B under SEM-BSE view at H2 (sample H2-Dol-Min). **C.** Cluster mineralization showing needles and fusiform pyrolusite in gallery 63 under NAPL. **D.** Raman spectra for pyrolusite in gallery 63 (63-01_3D1, 63-01_2D1) and between Hamaraouet and Aïn Beida (HA; HAB_1D1). **E.** Pyrolusite growing onto early botryoidal goethite generation in gallery 63 under NAPL. **F.** Pyrolusite and cryptomelane crossing hausmannite crystals and Dol-3 under SEM-BSE view at Hamaraouet (H1-Min2). Hausmannite is partly weathered into chalcophanite. Note that pyrolusite, in turn, seems to partly weathers into cryptomelane. **G.** Late botryoidal goethite brecciated by Dol-3A generation under SEM-BSE view at Hamaraouet. Note that late goethite grows onto the pyrolusite-calcite matrix. **H.** SEM-BSE view of hausmannite filled by Dol-3b and pyrolusite. Hollandite partly replaces pyrolusite. Dol=dolomite, Cal=calcite, Py=pyrolusite, Cph=chalcophanite, Hs=hausmannite, Cry=cryptomelane, Gth=goethite, Hol=hollandite.

Fig. 7 (color). Petrographic views of main mineralization types. **A.** Mixing of different Mn oxides (hausmannite, pyrolusite, cryptomelane, chalcophanite) within the host dolostone in Hamaraouet (H1) under PPL. **B.** Zoom of Fig. 6A under SEM-BSE showing hausmannite replaced by chalcophanite and cryptomelane. Pyrolusite occurs between hausmannite crystals. Note that Dol-3 is broken by cryptomelane. **C.** SEM-BSE view showing phase relation between hausmannite and manganite crossed by Mn carbonate (Ca-rhodochrosite) at Aïn Beida (AB). **D.** SEM-BSE view of crest-like barite associated with manganite and late Mn carbonate at Aïn Beida (AB). **E.** Massive late goethite generation growing onto hummocky pyrolusite in Hamaraouet (H4). Dol=dolomite, Cal=calcite, Py=pyrolusite, Cph=chalcophanite, Hs=hausmannite, Cry=cryptomelane, Gth=goethite, Mnt=manganite, Ba=barite, Rh=rhodochrosite.

Fig. 8 (black and white). Average integral crystallites of goethite (A) and hematite (B) samples.

Fig. 9 (color). Geochemistry of dolomite generations (Table 4). **A.** Composition of cement dolomite in the host rock. **B.** Composition of vein-filling dolomite. **C.** Distribution of MnO and FeO of dolomite in various geological settings. The Bou Arfa dolomite generations display an individual trend toward low FeO/MnO ratio.

Fig. 10 (color). Trace element pattern of whole rock analyses in the Mn (A) and Fe (B) ores (Tables 2 and 3).

Fig. 11 (color). Stable isotope (Table 7) plot to show the trend of progressive dolomitization in the Bou Arfa Mn deposit. Data from MVT deposits (Bouabdellah et al., 2012; Rddad, 2021; Rddad et al., 2018; Rddad and Bouhlel, 2016), Mn Imini deposit (Force et al., 1986) and shallow Mn-rich dolomite (Burns and Baker, 1987) are included.

Fig. 12 (black and white). A. PCA statistical distribution of chemical elements in the Bou Arfa deposit. **B-C.** Discrimination plot (Nicholson, 1992) between hydrothermal, supergene and dubhite Mn accumulation.

TABLES

Table 1. Description and location (Fig. 1B) of the studied samples. The mineralogy is referred as Qz=quartz, Fds=feldspars, Zr=zircon, Ap=apatite, Musc=muscovite, Dol=dolomite, Bt=biotite, Fe-Ti Ox.= Fe-Ti oxides, Py=pyrolusite, Hs=hausmannite, Fe-ox= Fe oxyhydroxides, Cph=chalcophanite, Cpm=cryptomelane, Cal=calcite, Hem=hematite, Goe=goethite, Hol=hollandite, Ba=barite. The main minerals are in bolt. WRA is the whole rock analysis.

Table 2. Whole rock geochemistry (major and trace elements) of the host and basement rocks given in wt.% (major oxides and LOI) and ppm (traces). <D.L. is under detection limit. LOI is the lost on ignition.

Table 3. Whole rock geochemistry (major and trace elements) of the Mn and Fe ores rocks given in wt.% (major oxides and LOI) and ppm (traces). <D.L. is under detection limit. LOI is the lost on ignition.

Table 4. EPMA analyses of different carbonate phases. The average values are given with their minimum (min) and maximum (max) values. The number of analyses is mentioned (=n). Standard deviation is also indicated for each batch and for the instrument (σ). D.L. is the detection limit. Standard list can be found in the data repository.

Table 5. EPMA analyses of Mn oxides: hausmannite and pyrolusite in Hamaraouet, and supergene cryptomelane, hollandite and chalcophanite. The number of analyses is

mentioned (=n). The average values are given. Standard deviation is also indicated for each batch and for the instrument (σ). D.L. is the detection limit. Standard list can be found in the data repository. Standard list can be found in the data repository.

Table 6. EPMA analyses of different Fe oxides. The number of analyses is mentioned (=n). The average values are given. Standard deviation is also indicated for each batch and for the instrument (σ). D.L. is the detection limit. Standard list can be found in the data repository.

Table 7. $\delta^{13}C$ and $\delta^{18}O$ compositions of dolomite in the Bou Arfa deposit. See Fig. 1B for the location of the studied samples.

Table 8. Key identification criteria of the dolomite generations under cathodoluminescence (CL)and light microscopy (LM).

Table 9. Cell dimensions of four goethite in Hamaraouet (Fig. 2) following the three main cell orthorhombic axis. The error is calculated according to the deviation of the experimental peak from the standard value.

Supplementary data repository

DR1. Analytical conditions standards of the EPMA CAMECA SX-five analyses.

DR2. Peak features in the XRD patterns of botryoidal hematite (H3_Hem) and across the massive goethite vein (H3_Gth6-9).

Highlights

- The Bou Arfa Mn(-Fe) mineralization (High Atlas, Morocco) is formed by post-sedimentary processes
- Dolomitization is considered as the main driver for Mn and Fe concentration
- The stability of the Mn(-Fe)-bearing minerals disabled strong post-ore weathering
- The proposed metallogenic model is similar to the genesis of Atlasic MVT deposits